



HAL
open science

Ultrafast Photoinduced Electron Transfers in Platinum(II)-Anthraquinone Diimine Polymer/PCBM Films

Frank Juvenal, Hu Lei, Adrien Schlachter, Paul-Ludovic Karsenti, Pierre
Harvey

► **To cite this version:**

Frank Juvenal, Hu Lei, Adrien Schlachter, Paul-Ludovic Karsenti, Pierre Harvey. Ultrafast Photoinduced Electron Transfers in Platinum(II)-Anthraquinone Diimine Polymer/PCBM Films. *Journal of Physical Chemistry C*, 2019, 123 (9), pp.5289-5302. 10.1021/acs.jpcc.9b00334 . hal-04632297

HAL Id: hal-04632297

<https://hal.science/hal-04632297v1>

Submitted on 18 Aug 2024

HAL is a multi-disciplinary open access archive for the deposit and dissemination of scientific research documents, whether they are published or not. The documents may come from teaching and research institutions in France or abroad, or from public or private research centers.

L'archive ouverte pluridisciplinaire **HAL**, est destinée au dépôt et à la diffusion de documents scientifiques de niveau recherche, publiés ou non, émanant des établissements d'enseignement et de recherche français ou étrangers, des laboratoires publics ou privés.

Ultrafast Photoinduced Electron Transfers in Platinum(II)-Anthraquinone Diimine Polymer/PCBM Films

Frank Juvenal, Hu Lei, Adrien Schlachter, Paul-Ludovic Karsenti, and Pierre D. Harvey*

Département de chimie, Université de Sherbrooke, Sherbrooke, PQ, Canada J1K 2R1

Abstract

Two fluorescent polymers ($[\text{Pt}]\text{-(AQI(BMPA)}_x)_n$) ($[\text{Pt}] = \textit{trans}$ -bis(ethynylbenzene)-bis(tributylphosphine)platinum(II); **AQI** = anthraquinone diimine; **BMPA** = bis(*para*-methoxyphenyl)amine), **P1** ($x = 1$; $\tau_F \leq 8$ ps) and **P2** ($x = 2$; $\tau_F = 10$ ps, 298 K), were prepared and investigated as thin films in the presence of phenyl- C_{61} -butyric acid methyl ester (PCBM) to probe the photoinduced electron transfer processes using steady-state and time-resolved fluorescence and femtosecond-transient absorption spectroscopy (fs-TAS). **P1** and **P2** undergo an efficient oxidative photoinduced electron transfer ($\text{P}x^* + \text{PCBM} \rightarrow \text{P}x^{+*} + \text{PCBM}^{-*}$; $x = 1, 2$) in solution and as films. Based on fs-TAS, the time scale for the photogenerated charge separated state forms within the excitation pulse (i.e., ≤ 150 fs). During the course of this study, the nature of the lowest energy emissive excited state was identified as a charge transfer state defined as $[\text{Pt}] \rightarrow \text{AQI}$ (major component) and $\text{BMPA} \rightarrow \text{AQI}$ (minor component) with the aid of density functional theory (DFT) and time-dependent DFT computations.

Introduction

The *trans*-bisethynylbis(trialkylphosphine)platinum(II) building block, $[\text{Pt}]$, is a versatile unit for the design of photonic materials showing potential applications in nonlinear optics (1–12) and light-emitting diodes. (13–20) In the field of solar cells, the $[\text{Pt}]$ -containing materials are also active irrespective of whether they are used as molecules or within polymer chains. (21,22) Indeed, dye-sensitized solar cells (23–26) and bulk heterojunction solar cells (BHJSCs) (27–34) were designed. To the best of our knowledge, the highest photoconversion efficiency (PCE) was recently reported to be 5.29% for a BHJSC containing the $[\text{Pt}]$ moiety. (35,36) Concurrently, studies on complexes bearing $[\text{Pt}]$ units indicated that the charge separated states are formed in the short picosecond (ps) time scale (37–40) and that the $[\text{Pt}]$ unit could mediate the electron transfer. (37–40) Over the years, it was suggested that anchoring diphenylamine pendants as electron-rich groups (41,42) and using the electron-deficient anthraquinone, **AQ**, moiety (43,44) should improve the PCEs of $[\text{Pt}]$ -containing materials for solar cells. Alternatively to $([\text{Pt}]\text{-[AQ]})_n$ polymers, (45) polymers containing

anthraquinone diimine, **AQI** (i.e., $([\text{Pt}]-[\text{AQI}]_n)$), were also designed. (46,47) These latter materials are nonemissive at room temperature (RT), but exhibit both low potential oxidation and reduction processes, (46,47) rendering them suitable for photoinduced electron transfers processes. Despite the fact that **[Pt]** is a common synthon and its relevance to its use in solar cells, there is, to the best of our knowledge, no investigation reporting the rates of photoinduced electron transfer between **[Pt]** and an electron acceptor. We now report an electron transfer study on $([\text{Pt}]-[\text{AQI}]_n)$ polymers (**P1**, **P2**; Chart 1) with 6,6-phenyl-C₆₁-butyric acid methyl ester (PCBM). These polymers are found fluorescent, a property that was never observed before for this type of chromophore, including quinone diimine (**QI**) polymers, $([\text{Pt}]-[\text{QI}]_n)$, (48–53) which provide an extra analytical signal for the study of electron transfer. Femtosecond-transient absorption spectroscopy (fs-TAS) performed on 1:1 **P1**/PCBM and **P2**/PCBM films indicates that the lifetimes of all transient signals (neutral and charged PCBM, **P1** and **P2**) are generated within the laser pulse (i.e., ≤ 150 fs) translating into ultrafast electron transfer rates, $k_{\text{et}} \geq 6.6 \times 10^{12} \text{ s}^{-1}$.

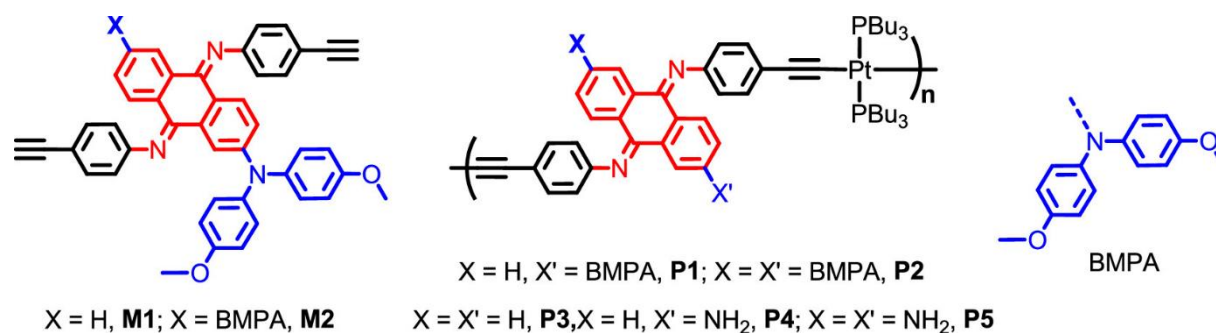


Chart 1. Structures of **M1**, **M2**, **P1**, **P2**, and Literature Polymers (**P3–5**) (46,47) Discussed in This Work

Experimental Section

Materials

Compounds *trans*-PtCl₂(PBu₃)₂ (38) and 4-[(trimethylsilyl)ethynyl] (54) were prepared according to literature procedures. TiCl₄, 1,4-diazabicyclo[2.2.2]octane (DABCO), ethynyltrimethylsilane, CuI, bis(4-methoxyphenyl)amine (BMPA), sodium *tert*-butoxide (*t*-BuONa), 2-bromoanthracene-9,10-dione, 2,6-dibromoanthracene-9,10-dione, phenyl-C₆₁-butyric acid methyl ester (PCBM), [1,3-bis(2,6-diisopropylphenyl)imidazol-2-ylidene](3-chloropyridyl)palladium(II) dichloride (PEPPSI-IPr), and PdCl₂(PPh₃)₂ were purchased from Aldrich and were used as received. All flasks were dried under a flame to eliminate moisture.

Solvents were distilled from appropriate drying agents, and other reagents were used as received.

Syntheses of 2a and 2b

2a: 2-Bromoanthracene-9,10-dione (860 mg, 3.0 mmol), bis(4-methoxyphenyl)-amine (0.76 g, 3.3 mmol), PEPPSI-IPr (0.08 g, 0.1 mmol), and sodium *tert*-butoxide (0.72 g, 7.5 mmol) were added into dry toluene (30 mL). The mixture was stirred at 100 °C for 12 h. Water (100 mL) was added to the cooled mixture and stirred for 20 min at room temperature (RT). The precipitant was filtered and washed with methanol and then a crude product (1.07 g, yield: 82%) was obtained. The crude product was purified by column chromatography on silica gel to give the product. **2b:** A procedure similar to that used for **2a** was followed but with 2,6-dibromoanthraquinone (1.10 g, 3.0 mmol) instead of 2-bromoanthracene-9,10-dione. After purification by vacuum sublimation, a red solid (1.20 g, 60%) was produced.

2a

¹H NMR (300 MHz, CDCl₃) δ 8.33–8.27 (m, 1H), 8.25–8.19 (m, 1H), 8.10 (d, *J* = 8.8 Hz, 1H), 7.76 (pd, *J* = 7.3, 1.6 Hz, 2H), 7.64 (d, *J* = 2.6 Hz, 1H), 7.21–7.16 (m, 4H), 7.13 (dd, *J* = 8.8, 2.6 Hz, 1H), 6.99–6.88 (m, 4H), 3.86 (s, 6H). Matrix-assisted laser desorption ionization time-of-flight (MALDI-TOF): *m/z* calcd C₂₈H₂₃NO₄ (M) 437.16, found 437.16.

2b

¹H NMR (300 MHz, CDCl₃) δ 7.99 (d, *J* = 8.7 Hz, 2H), 7.62 (d, *J* = 2.6 Hz, 2H), 7.20–7.12 (m, 8H), 7.04 (dd, *J* = 8.7, 2.6 Hz, 2H), 6.96–6.87 (m, 8H), 3.85 (s, 12H). MALDI-TOF: *m/z* calcd C₄₂H₃₆N₂O₆ (M) 664.26, found 664.24.

Syntheses of 3a and 3b

3a: Compound **2a** (436 mg, 1 mmol) and 450 mg (4.0 mmol) of DABCO were dissolved in 50 mL of chlorobenzene while heating to 90 °C. TiCl₄ (0.24 mL, 2.2 mmol) was added dropwise, followed by the addition of 4-((trimethylsilyl)ethynyl)-aniline (416 mg, 2.2 mmol) and rinsing the powder addition funnel with 5 mL of chlorobenzene. The solution was stirred at 115 °C for a 2 h period. The product was isolated by filtering off the precipitate and washed with hot chlorobenzene (2 × 10 mL). The solution was evaporated. The solid was dissolved in CHCl₃, washed three times with water, dried with MgSO₄, and filtered. The CHCl₃ was completely evaporated, leaving only the product. The product was purified on a silica column to give the compound **3a** (500 mg, 64%). **3b:** A procedure similar to that used for **3a** was followed. After

purification by vacuum sublimation, a red solid (580 g, 58%) was produced. **3a**: ^1H NMR (300 MHz, CDCl_3) δ 8.20 (dd, $J = 37.3, 30.1$ Hz, 2H), 7.78–7.31 (m, 6H), 7.09 (s, 3H), 6.85 (d, $J = 18.3$ Hz, 10H), 6.68 (d, $J = 7.6$ Hz, 1H), 6.50 (d, $J = 44.4$ Hz, 1H), 3.85 (s, 6H), 0.29 (d, $J = 6.0$ Hz, 18H). MALDI-TOF: m/z calcd $\text{C}_{50}\text{H}_{49}\text{N}_3\text{O}_2\text{Si}_2$ (M) 779.34, found 779.32. **3b**: ^1H NMR (300 MHz, CDCl_3) δ 8.00 (dd, $J = 8.7, 5.1$ Hz, 1H), 7.68 (dd, $J = 18.1, 16.0$ Hz, 1H), 7.41 (d, $J = 7.3$ Hz, 2H), 7.31 (s, 2H), 7.20–6.99 (m, 6H), 6.88 (dd, $J = 17.3, 8.4$ Hz, 15H), 6.56 (dd, $J = 47.2, 30.1$ Hz, 3H), 3.93–3.73 (m, 12H), 0.28 (s, 18H). MALDI-TOF: m/z calcd $\text{C}_{64}\text{H}_{62}\text{N}_4\text{O}_4\text{Si}_2$ (M) 1006.43, found 1006.41.

Syntheses of M1 and M2

M1: To a 100 mL round-bottom flask was added 20 mL of dichloromethane (DCM)/MeOH (v/v = 2:1). The solvents were purged with argon before addition of **3a** (400 mg, 0.5 mmol); K_2CO_3 (4 mL, 4 mmol) was then added. The reaction was stirred for 2 h prior to filtering off the salt under vacuum. Chromatography on silica gel afforded the target compound **M1** (293 mg, 90%). **M2**: A procedure similar to that used for **M1** was followed. After purification by vacuum sublimation, a red solid (294 g, 86%) was produced. **M1**: ^1H NMR (300 MHz, CDCl_3) δ 8.22 (t, $J = 33.2$ Hz, 2H), 7.81–7.30 (m, 6H), 7.10 (s, 3H), 6.86 (d, $J = 23.8$ Hz, 10H), 6.70 (d, $J = 7.7$ Hz, 1H), 6.53 (d, $J = 38.8$ Hz, 1H), 3.85 (s, 6H), 3.12 (d, $J = 20.5$ Hz, 2H). MALDI-TOF: m/z calcd $\text{C}_{44}\text{H}_{33}\text{N}_3\text{O}_2$ (M) 635.26, found 635.25. **M2**: ^1H NMR (300 MHz, CDCl_3) δ 8.00 (dd, $J = 8.7, 5.1$ Hz, 1H), 7.68 (dd, $J = 18.1, 16.0$ Hz, 1H), 7.41 (d, $J = 7.3$ Hz, 2H), 7.31 (s, 2H), 7.20–6.99 (m, 6H), 6.88 (dd, $J = 17.3, 8.4$ Hz, 15H), 6.56 (dd, $J = 47.2, 30.1$ Hz, 3H), 3.93–3.73 (m, 12H), 3.11 (d, 2H). MALDI-TOF: m/z calcd $\text{C}_{58}\text{H}_{46}\text{N}_4\text{O}_4$ (M) 862.35, found 862.33.

Syntheses of P1 and P2

P1: To a 50 mL Schlenk tube was added 30 mL of DCM and 5 mL of Et_3N ; the solvents were purged with argon for 10 min before addition of compound **M1** (250 mg, 0.4 mmol) or **M2** (220 mg, 0.4 mmol) and *trans*- $\text{PtCl}_2(\text{PBu}_3)_2$ (268 mg, 0.4 mmol). The resulting solution was stirred at 298 K overnight. After complete conversion of the starting materials as monitored by thin-layer chromatography, the solvent was evaporated. The product was dissolved into 5 mL of DCM, and then 30 mL of methanol was added to get the precipitation. The above procedure was recycled three times to get the final product **P1** (218 mg, 42%). **P2**: A procedure similar to that used for **P1** was followed. After purification by vacuum sublimation, a red solid (116 g, 38%) was produced. **P1**: ^1H NMR (300 MHz, CDCl_3) δ 8.32, 8.19, 7.73, 7.55, 7.23, 7.11, 6.89,

6.86, 6.85, 6.81, 6.73, 6.69, 6.66, 2.20, 1.65, 1.51, 1.48, 1.46, 1.43, 0.96, 0.94, 0.91. ^{31}P NMR (122 MHz, CDCl_3) δ 2.72 ($J_{\text{P-Pt}} = 2370$ Hz). Gel permeation chromatography (GPC): $M_n = 5240$ Da, $M_n/M_w = 2.07$. Chem. anal. for $\text{C}_{68}\text{H}_{84}\text{N}_3\text{O}_2\text{P}_2\text{Pt}\cdot\text{H}_2\text{O}$ (theory): C 65.25; H 6.87; N 3.36%. Found: C 64.98; H 6.84; N 3.34%. **P2**: ^1H NMR (300 MHz, CDCl_3) δ 8.01, 7.98, 7.81, 7.75, 7.68, 7.63, 7.22, 7.11, 7.08, 6.93, 6.91, 6.89, 6.87, 6.86, 6.84, 6.80, 6.76, 6.63, 6.37, 3.82, 2.18, 1.51, 1.48, 1.46, 1.44, 0.94, 0.92, 0.89. ^{31}P NMR (122 MHz, CDCl_3) δ 2.85 ($J_{\text{P-Pt}} = 2370$ Hz). GPC: $M_n = 4446$ Da, $M_n/M_w = 1.69$. Chem. anal. for $\text{C}_{82}\text{H}_{97}\text{N}_4\text{O}_4\text{P}_2\text{Pt}\cdot\text{H}_2\text{O}$ (theory): C 66.58; H 6.70; N 3.79%. Found: C 65.68; H 6.54; N 3.97%. Evidence for water is found in the ^1H NMR spectra.

Instruments

The ^1H , ^{13}C , and ^{31}P NMR spectra were collected on a Bruker DRX400 spectrometer using the solvent as a chemical shift standard. The coupling constants are in hertz. MALDI-TOF mass spectra were recorded on a Bruker BIFLEX III TOF mass spectrometer (Bruker Daltonics, Billerica, MA) using a 337 nm nitrogen laser with dithranol as the matrix. The spectra were measured from freshly prepared samples. All these spectra are provided in Figures S1–S17. The absorption spectra in the solution were measured on a Varian Cary 300 Bio UV–vis spectrometer at 298 K and on a Hewlett-Packard 8452A diode array spectrometer with a 0.1 s integration time at 77 K. The steady-state fluorescence (<820 nm) and the corresponding excitation spectra were acquired on an Edinburgh Instruments FLS980 phosphorimeter equipped with single monochromators, whereas steady-state near-infrared (NIR) emissions were measured by a QuantaMaster 400 phosphorimeter from Photon Technology International upon excitation by a xenon lamp and recording with a NIR PMT-7-B detector. Fluorescence lifetime measurements were made with the FLS908 spectrometer using a 378 nm picosecond (ps) pulsed diode laser (full width at half-maximum (fwhm) = 78 ps) as an excitation source. Data collection on the FLS980 system was performed using time correlated single photon counting (TCSPC). All fluorescence spectra were corrected for instrument response. All measurements at 77 K were performed with an EPR Dewar assembly using an NMR tube of diameter of ~ 5 mm (i.e., 4.947 ± 0.019 mm). The fluorescence lifetimes were extracted from either multiexponential analyses or the exponential series method (ESM). (55,56)

Film Preparation

Solutions of **P1**, **P2**, PCBM, **P1/PCBM**, and **P2/PCBM**, typically 10^{-3} M in CH_2Cl_2 , were spun at 3000 rpm for 1 min with a spin coater from Speciality Coating System, 6800 Spin Coater

Series. The average thickness of the films was $\sim 50 \pm 2$ nm and was measured on a KLA-Tencor Profiler, AlphaStep D-120.

Femtosecond Transient Absorption Spectroscopy (fs-TAS)

The fs-transient spectra and decay profiles were acquired on a homemade system using the SHG of a Solstice (Spectra Physics) Ti:sapphire laser ($\lambda_{\text{exc}} = 398$ nm; fwhm = 75 fs; pulse energy = 0.1 μ J per pulse, rep. rate = 1 kHz; spot size ~ 500 μ m), a white light continuum generated inside a sapphire window, and a custom-made dual charge-coupled device camera of 64×1024 pixels sensitive between 200 and 1100 nm (S7030, Spectronic Devices). The delay line permitted one to probe up to 4 ns with an accuracy of ~ 4 fs. The results were analyzed with the program Glotaran (<http://glotaran.org>) permitting one to extract a sum of independent exponentials ($I(\lambda, t) = C_1(\lambda) e^{-t_1/\tau} + C_2(\lambda) e^{-t_2/\tau} + \dots$) that fits the whole three-dimensional transient map.

Fast Kinetic Fluorescence Measurements

The short components of the fluorescence decays were measured using the output of an optical parametric amplifier (OPA-800CF, Spectra-Physics) operating at $\lambda_{\text{exc}} = 490$ nm, a pulse width of 90 fs, rep. rate = 1 kHz, pulse energy = 1.6 μ J per pulse, spot size ~ 2 mm, and a streak camera (AXIS-TRS, Axis Photonique Inc.) with less than 8 ps resolution. The results were also globally analyzed with the program Glotaran (<http://glotaran.org>) permitting one to extract a sum of independent exponentials ($I(\lambda, t) = C_1(\lambda) e^{-t_1/\tau} + C_2(\lambda) e^{-t_2/\tau} + \dots$). The resulting time-resolved spectra are not corrected for the instrument response.

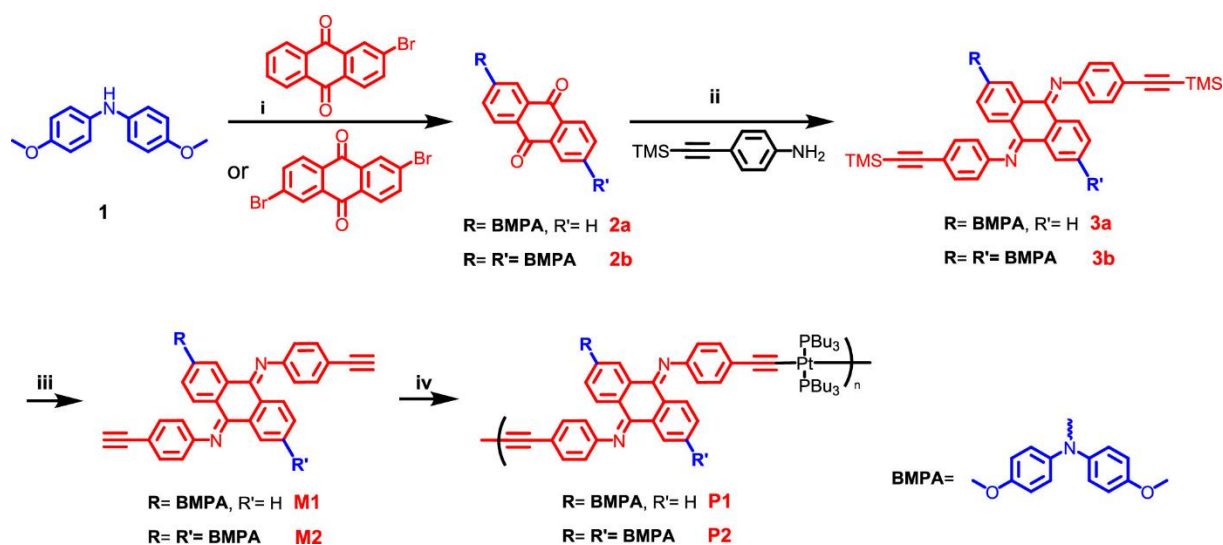
Computations

All density functional theory (DFT) calculations were performed with Gaussian 09 (57) at the Université de Sherbrooke with the Mammoth supercomputer supported by Le Réseau Québécois De Calculs Hautes Performances. The DFT geometry optimizations and time-dependent DFT (TDDFT) calculations (58–67) were carried out using the B3LYP method. A 6-31g* basis set was used for C, H, N, and O atoms. (68–73) Valence double ζ with SBKJC effective core potentials was used for all Pt atoms. (68–73) Theoretical UV–visible absorption spectra were obtained using GaussSum 3.0. (74)

Results and Discussion

Synthesis

The syntheses of polymers **P1**, **P2** and their models **M1**, **M2** are shown in Scheme 1. Compounds **2a** and **2b** were obtained through a Buchwald–Hartwig coupling reaction between **1** with 2-bromoanthracene-9,10-dione (**2a**) and 2,6-dibromoanthracene-9,10-dione (**2b**). **3a** and **3b** were obtained by reacting **2a** or **2b** with 4-((trimethylsilyl)-ethynyl)aniline, respectively, under the catalysis of TiCl_4 in chlorobenzene at 115 °C with the DABCO as the base. After removal of the trimethylsilyl groups, **M1** and **M2** reacted, respectively, with *trans*- $\text{PtCl}_2(\text{PBu}_3)_2$ and CuI as the catalysts at 298 K in CH_2Cl_2 to, respectively, provide polymers **P1** and **P2**. The NMR and MALDI-TOF spectra are shown in Figures S1–S16.



Scheme 1. Syntheses of **P1**, **P2** and Their Models **M1**, **M2**^a

^aReagents and conditions: (i) cat. Pd, *t*-BuONa, toluene, 100 °C, 12 h, 60%; (ii) TiCl_4 , DABCO, $\text{C}_6\text{H}_5\text{Cl}$, 115 °C, 2 h, 58%; (iii) K_2CO_3 , DCM/MeOH, 298 K, 2 h, 86%; and (iv) *trans*- $\text{PtCl}_2(\text{PBu}_3)_2$, CuI , Et_3N , DCM, 298 K, 12 h, 38%.

The formation of polydispersed oligomers **P1** and **P2** ($M_n = 5240$ (four units) and 4446 (three units); $M_w/M_n = 2.077$ and 1.693) and their models **M1** and **M2** was confirmed by ^1H and ^{31}P NMR spectroscopies (note that the $J_{\text{P-Pt}}$ value (2370 Hz) is indicative of a *trans*-geometry about the Pt) and GPC. The use of oligomers as models for polymers is appropriate since electronic communication does not generally exceed a few units in **[Pt]**-containing materials. (75)

Absorption Spectra and DFT and TDDFT Computations

P1 and **P2** were found fluorescent from the lowest energy excited state at room temperature, thus drastically contrasting with the **([Pt]-[AQ])_n**, (45) **([Pt]-[QI])_n**, (48–53) and **([Pt]-[AQI])_n** (38,54) polymers reported to be nonemissive or, at best, only luminescent in glassy

matrices at 77 K. The absorption, excitation, and fluorescence spectra of **2a**, **2b**, **M1**, **M2**, **P1**, and **P2** in 2MeTHF at 298 K are presented in Figure 1, and the absorptivity data are summarized in Table 1. From an examination of the tails, where the 0–0 peak positions are expected (i.e., these tails spread, respectively, from ~500 to ~550 nm and from ~525 to ~575 nm for **M1** and **M2** and from ~550 to ~600 and from ~550 to ~625 nm for **P1** and **P2**, respectively), it is concluded that the 0–0 peak positions should be placed at lower energy for **P1** and **P2** in comparison with **M1** and **M2**. This conclusion is fully consistent with the calculated positions presented below. The corresponding spectra at 77 K are shown in Figure S17. The absorption spectra are characterized by a low-energy absorption band spreading from 400 to 600 nm and are similar to that reported by Wang et al. (46) for **AQI**-containing materials. The minor difference is that the band maxima are red-shifted by ~50 nm for the materials investigated in this work. The nature of the lowest energy singlet excited states is addressed by DFT computations for necessary confirmation purposes. The optimized geometry and frontier molecular orbital (MO) representations of the model compounds **2a**, **2b**, **M1**, and **M2** and fragments of **P1** and **P2** have been calculated (Figures 2–5). The relative atomic orbital contributions distributed as subfragments to the frontier MOs and the calculated positions of the 0–0 peaks, oscillator strengths, and their major contributions to the lowest energy electronic transitions (TDDFT) are provided in Tables 2 and 3.

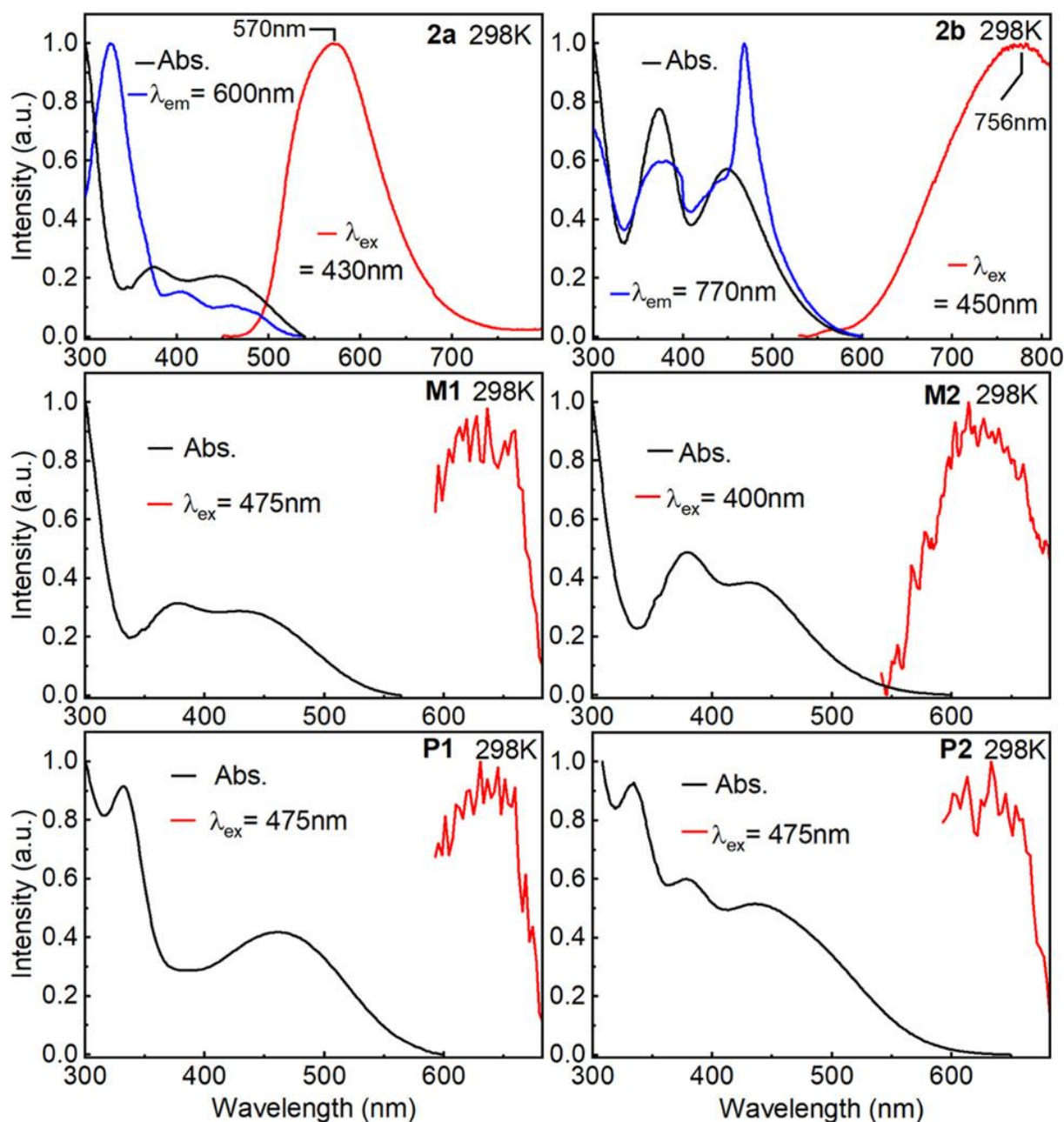


Figure 1. Absorption (black), excitation (blue), and emission (red) spectra for **2a**, **2b**, **M1**, **M2**, **P1**, and **P2** at 298 K in 2MeTHF (see Figure S17 for the 77 K data). Note that no excitation spectra measurement is possible with the fs laser/streak camera system (for **M1**, **M2**, **P1**, and **P2**, so the peak maxima should be somewhat more red-shifted). The sharp peak at 475 nm in the excitation spectrum of **2b** is an instrument artifact. The near-IR portion of the fluorescence spectrum of **2b** (using a near-IR detector) is provided in Figure S18.

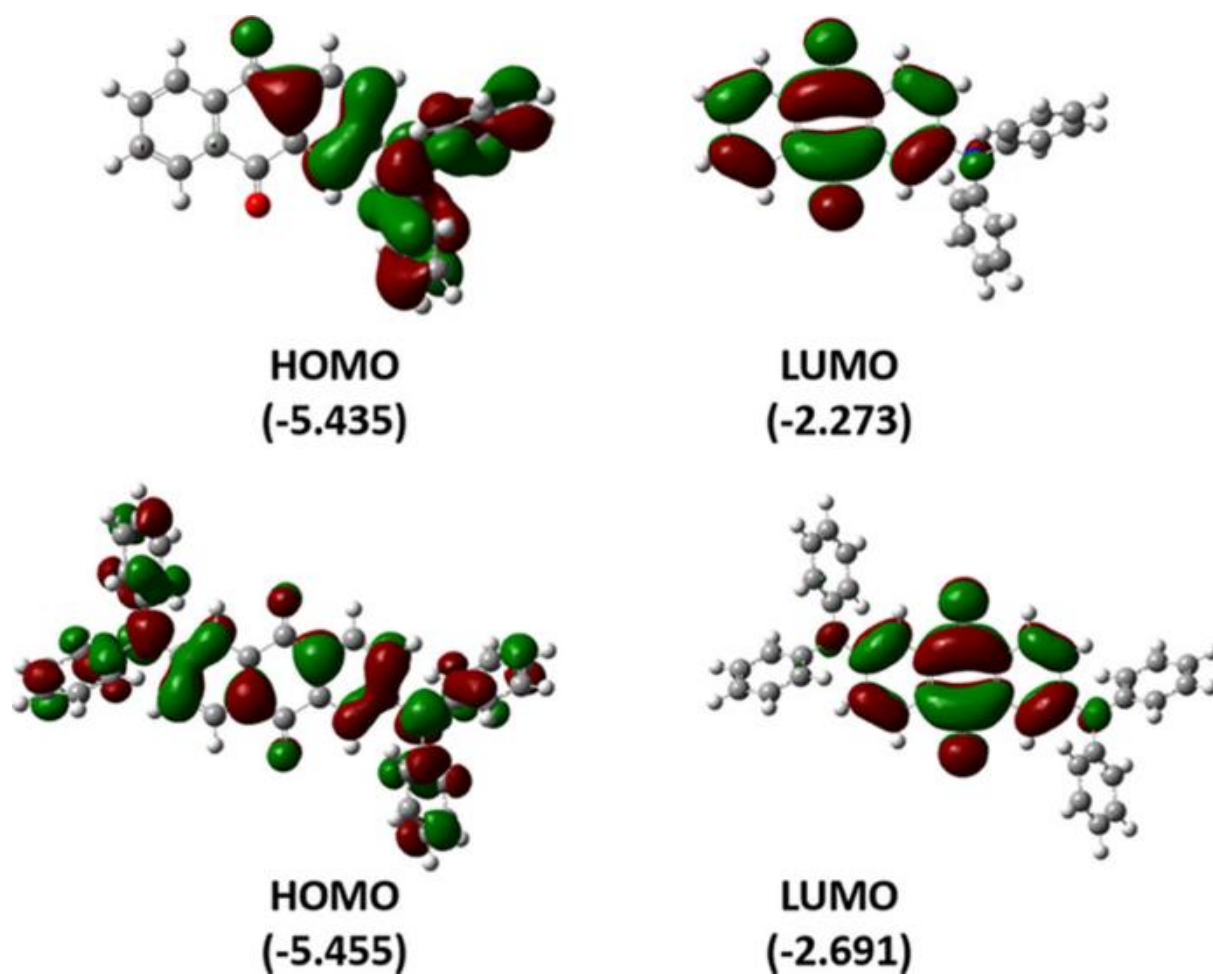


Figure 2. Representations of the frontier MOs of **2a** (up) and **2b** (down) based on an optimized geometry and using a tetrahydrofuran (THF) solvent field (energies in electronvolts). Red, positive isosurface; green, negative isosurface.

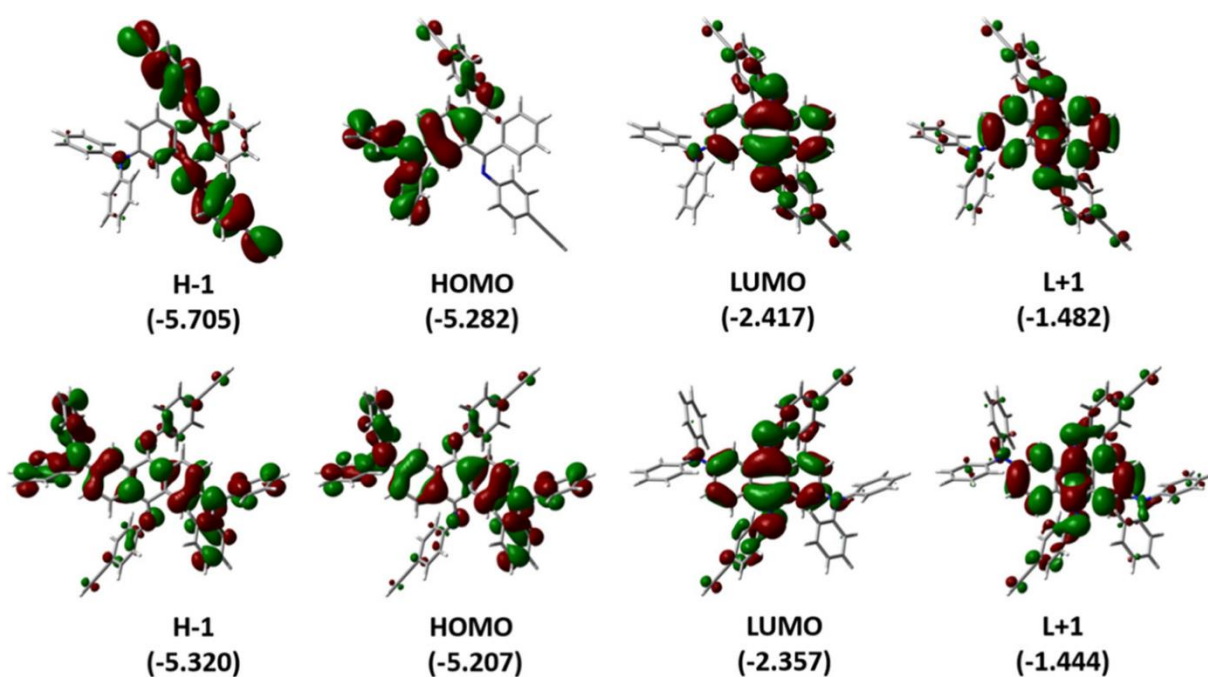


Figure 4. Representations of the frontier MOs of **P1** based on an optimized geometry and using a THF solvent field (energies in electronvolts). Red, positive isosurface; green, negative isosurface.

Table 1. Absorptivity Data of 2a, 2b, M1, P1, and P2 in 2MeTHF^a

compds	λ_{\max} (nm) (ϵ ($M^{-1} \text{ cm}^{-1}$))		
2a		374 (26 100)	443 (23 100)
2b		374 (19 700)	449 (15 800)
M1		377 (12 100)	440 (10 700)
M2^a		379	447
P1	331 (61 000)		461 (27 400)
P2	334 (34 700)	378 (21 200)	436 (19 600)

^aThe absorptivity data for **M2** were not measured.

Table 2. Relative Contributions (%) of the Various Fragments to the Frontier MOs of 2a, 2b, M1, M2, a Fragment of P1, and a Fragment of P2 (Values >50% Are Shown in Bold)

	H - 4	H - 3	H - 2	H - 1	HOMO	LUMO	L + 1	L + 2	L + 3	L + 4
2a										
AQ	91.0	58.0	82.9	8.6	28.9	96.1	93.2	63.4	27.6	31.0
BMPA	9.0	42.0	17.1	91.4	71.1	3.9	6.8	36.6	72.4	69.0
2b										
AQ	8.3	9.7	99.0	26.6	31.8	90.9	86.9	51.2	18.5	18.0
BMPA	91.7	90.3	1.0	73.4	68.2	9.1	13.1	48.8	81.5	82.0
M1										
AQI	67.8	24.7	96.4	96.7	36.0	97.1	95.4	94.6	83.9	71.6
BMPA	32.2	75.3	3.6	3.3	64.0	2.9	4.6	5.4	16.1	28.4
M2										
AQI	43.2	95.0	91.5	35.1	36.4	93.9	91.4	92.7	57.1	87.8
BMPA	56.8	5.0	8.5	64.9	63.6	6.1	8.6	7.3	42.9	12.2
Fragment of P1										
AQI	3.6	0.1	25.5	24.5	23.4	79.0	83.1	13.3	32.9	33.2
BMPA	0.8	0.0	56.8	4.5	9.2	2.9	4.9	5.7	63.5	60.1

	H - 4	H - 3	H - 2	H - 1	HOMO	LUMO	L + 1	L + 2	L + 3	L + 4
[Pt]	95.6	99.9	17.6	71.0	67.4	18.2	12.0	81.0	3.6	6.7
Fragment of P2										
AQI	1.7	24.1	26.1	26.8	22.0	76.4	79.2	12.6	50.1	19.6
BMPA	0.6	65.5	51.9	19.6	6.4	5.9	9.2	4.0	45.0	76.6
[Pt]	97.7	10.4	21.9	53.6	71.6	17.7	11.7	83.4	5.0	3.8

Table 3. Calculated Positions of the 0–0 Peaks, Oscillator Strengths (f), and Their Major Contributions for the Lowest Energy Electronic Transitions of 2a, 2b, M1, M2, a Fragment of P1, and a Fragment of P2^a

no.	λ (nm)	f	major contributions (%)	no.	λ (nm)	f	major contributions (%)
2b				2a			
1	555	0	HOMO \rightarrow LUMO (99)	1	552	0.154	HOMO \rightarrow LUMO (99)
2	521	0.472	H - 1 \rightarrow LUMO (99)				
M1				P1			
1	517	0.1858	HOMO \rightarrow LUMO (97)	1	561	0.5061	HOMO \rightarrow LUMO (95)
2	470	0.2899	H - 1 \rightarrow LUMO (94)	2	534	0.2078	H - 1 \rightarrow LUMO (94)
3	451	0.0337	H - 2 \rightarrow LUMO (93)	3	480	0.0826	H - 2 \rightarrow LUMO (96)
				4	426	0.0013	H - 3 \rightarrow LUMO (99)
M2				P2			
1	524	0.0454	HOMO \rightarrow LUMO (98)	1	560	0.5231	HOMO \rightarrow LUMO (94)
2	491	0.4195	H - 1 \rightarrow LUMO (95)	2	551	0.1566	H - 1 \rightarrow LUMO (95)
3	462	0.2434	H - 2 \rightarrow LUMO (92)	3	485	0.0096	H - 2 \rightarrow LUMO (96)
4	445	0.0217	H - 3 \rightarrow LUMO (94)	4	473	0.2777	H - 3 \rightarrow LUMO (96)

^aSee Tables S1–S6 for the tables containing the first 100 electronic transitions and Figure S19 for the corresponding simulated spectra.

An examination of the frontier MOs for the polymers (Figures 5 and 6) confirms that the nature of the lowest energy excited states is a charge transfer (CT) excited state of the type **[Pt]** \rightarrow **AQI** (again **[Pt]** = Pt(PBu₃)₂(C \equiv C)₂), which is consistent with what is expected. (46,47)

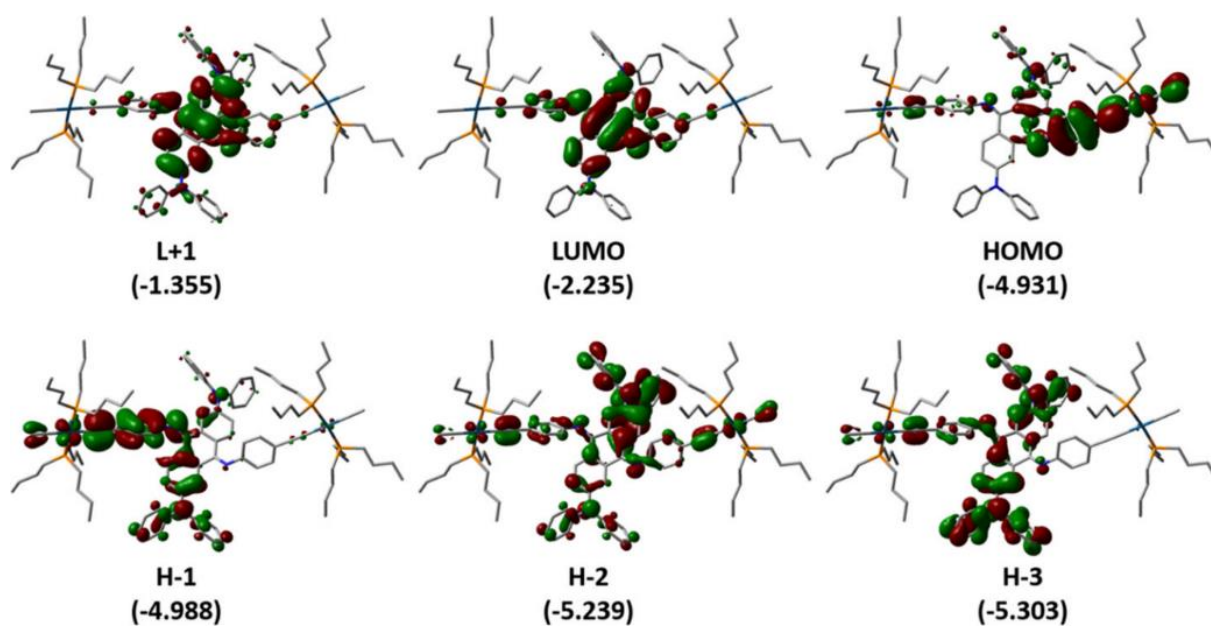


Figure 5. Representations of the frontier MOs of **P2** based on an optimized geometry and using a THF solvent field (energies in electronvolts). Red, positive isosurface; green, negative isosurface.

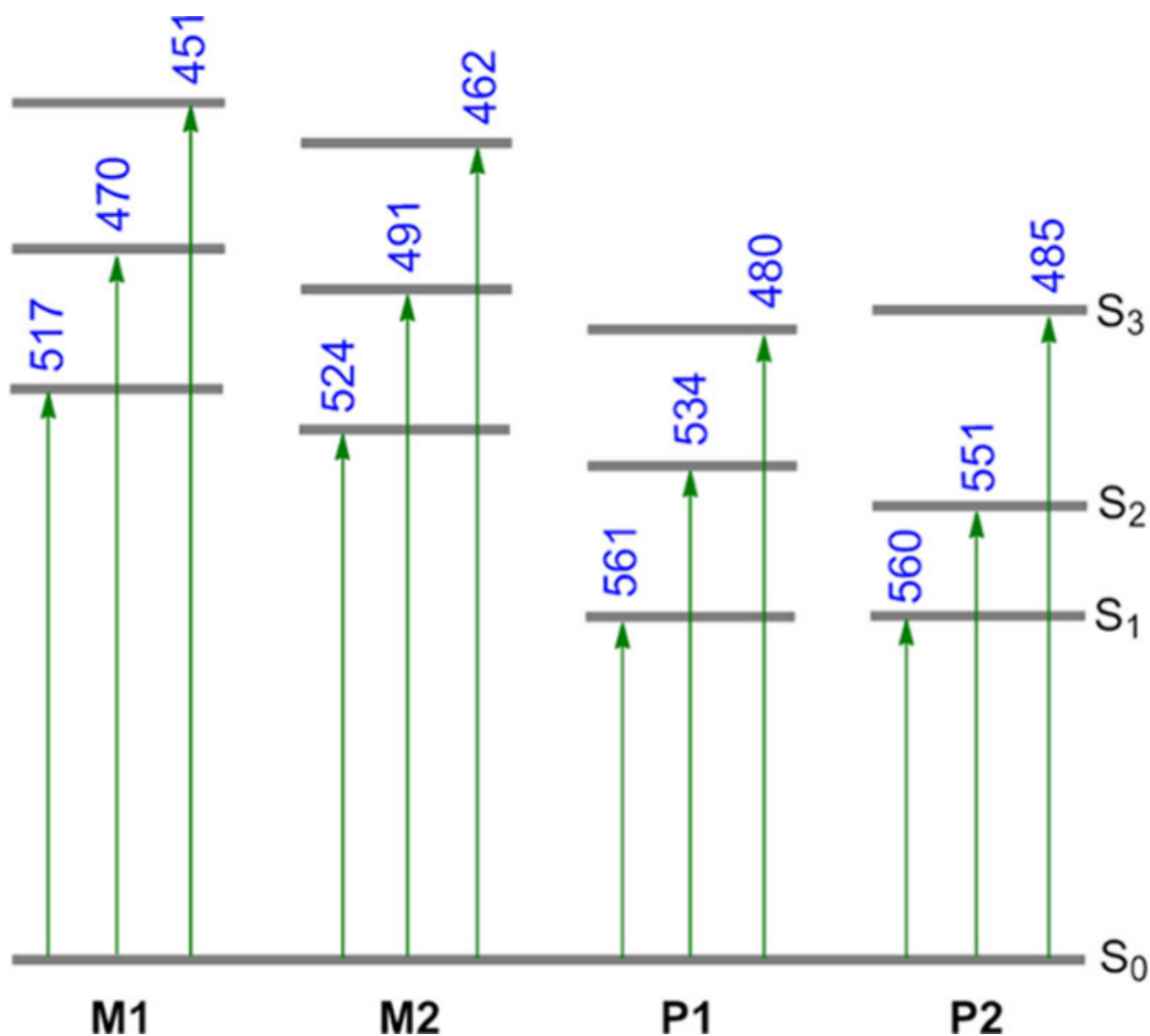


Figure 6. Comparison of the calculated state diagrams (TDDFT) for **M1**, **M2**, **P1**, and **P2**. The values in blue are the computed positions (in nanometers) of the pure (0–0) electronic transitions.

The lowest energy transition is also a CT process but involving mainly **[Pt]** → **AQI**, thus confirming that the nature of the S₁ state has not changed upon the anchoring of the electron-rich BMPA groups; a minor CT contribution from BMPA → **AQI** is also computed. Moreover, for confirmation purposes, the simulated absorption spectra were also obtained by TDDFT computations (Figure S19), and the correspondence with the general shape of the experimental spectra, excluding the vibronic contributions, is also noted.

The calculated energy diagrams for the lowest energy singlet excited states are shown in Figure 6. The four striking features are that (1) the lowest unoccupied molecular orbital (LUMO) exhibits atomic contributions located on **AQ** or **AQI** mainly, (2) the lowest energy electronic transitions are always highest occupied molecular orbital (HOMO) → LUMO with

a relative contribution $\geq 94\%$, (3) the calculated positions of the electronic transitions ($517 < \lambda < 561$ nm) always fall in the vicinity of the position where the absorption and fluorescence bands overlap (Figure 1), and (4) the HOMO exhibits atomic contributions located on [Pt] for **P1** and **P2**. For **2a**, **2b**, **M1**, and **M2**, the HOMO exhibits atomic contributions mainly located on the BMPA groups. In these cases, the lowest energy electronic transition produces a charge transfer (CT) excited state: BMPA \rightarrow **AQ** or **AQI**. Conversely, the HOMO of **P1** and **P2** exhibits atomic contributions mainly located on [Pt], which is relevant for the electron transfer study below. So, a HOMO \rightarrow LUMO transition leads to the decrease of the atomic contributions of both [Pt] and BMPA residues and increase of those for the **AQI**.

Fluorescence Spectra and Excited State Lifetimes

These species are strongly fluorescent at 77 K (**M1**, **M2**, and **P2**), all from the lowest energy excited state (Figure S17), and **P1** turns out to be only weakly fluorescent (a laser setup and a streak camera were needed to measure the spectrum). This result contrasts with the fact that **P3** and **P4** were not found emissive from the CT S_1 state (i.e., the CT state $^1([\text{Pt}] \rightarrow \text{AQI})^*$) at all. (46,47) At 298 K, weak emissions have been detected (with a streak camera) in the CT $^1([\text{Pt}] \rightarrow \text{AQI})^*$ region for **M1**, **M2**, **P1**, and **P2** (Figure 1). Because the intensity is so weak, no reliable fluorescence quantum yield (Φ_F) could be measured ($\Phi_F < 0.0001$; the detection limit). This situation corroborates the short S_1 lifetimes extracted from the streak camera and fs-transient absorption spectra (below).

Noteworthy, **2a** (narrow, 570 nm) and **2b** (broad, 756 nm) exhibit distinctively different fluorescence maxima at 298 K. This phenomenon has previously been described for 2,6-bis(diphenylamino)anthraquinone at 298 K (i.e., a structure similar to compound **2b** but without the methoxy groups). (76) The Stoke shift for **2b** (9000 cm^{-1} in 2MeTHF) resembles that for 2,6-bis(diphenylamino)anthraquinone (7400 cm^{-1} in THF). (76) In the latter case, a low-lying twisted charge separated state (TCSS) can be formed depending on the medium polarity, which lasts for many ps (~ 13 ps). As deduced by DFT computations, the presence of the methoxy groups enhances the electron-donor ability of the diphenylamino groups and so the emissive CT band for **2b** (756 nm) should be more red-shifted in comparison with 2,6-bis(diphenylamino)anthraquinone ($\lambda_{\text{Fluo}} \sim 650$ nm in THF), as observed. (76) **2a**, which bears only one BMPA group, does not exhibit this broad and red-shifted fluorescence ($\lambda_{\text{Fluo}} \sim 570$ nm in THF), suggesting the absence of TCSS. This observation is consistent with the fact that both **2a** and **2b** in rigid media in 77 K glasses where twisting is unlikely exhibit relatively blue-

shifted fluorescence bands (both at 644 ± 2 nm; Figure S17) with respect to that for **2b** at 298 K ($\lambda_{\text{Fluo}} = 756$ nm). This phenomenon was not studied in detail since it was not the scope of this investigation, but the presence of single N–C bonds suggests the possibility of having more than one emissive conformer. The nanosecond (ns) time scale of the emission lifetime (τ_{F}) at 77 K (measured by TCSPC, Table 4) and the smaller Stoke shift ($\sim 4500\text{--}6000$ cm^{-1}) further corroborate the fluorescence. Moreover, the excitation spectra exhibit a reasonable match, but not perfectly, with the absorptions.

Table 4. τ_{F} Data for 2a, 2b, M1, M2, P1, and P2 in 2MeTHF at 77 and 298 K^a

	λ (nm) ^b ax. 77 K	λ (nm) ^c oni. 77 K	τ_{F} (ns) (rel. contribution, %) ^d 77 K	χ^2	τ_{F} (ps) stre ak 298 K ^e	τ (S ₁) (ps) TAS 298 K
2a	642	650	0.73 (7), 2.67 (49), 7.67 (44)	1.04	$\leq 8^{\text{f}}$	—^{g}
2b	646	680	1.03 (8), 2.99 (62), 8.20 (30)	1.03	41	—^{g}
M1	686	680	0.036 (13), 0.59 (53), 2.25 (34)	1.00	9.3	—^{g}
M2	650	650	0.93 (7), 3.29 (60), 21.1 (33)	1.04	82	—^{g}
P1	630	630	$\leq 0.008^{\text{d}}$		$\leq 8^{\text{f}}$	9.9
P2	645	650	0.18 (5), 0.80 (5), 3.7 (36), 10.6 (54) ^h	1.04	10	10.4

^aThe uncertainties on τ_{F} and $\tau(\text{S}_1)$ are $\pm 5\text{--}10\%$ based on multiple measurements.

^bThe spectra are shown in Figure S17.

^cThese are the monitoring wavelengths.

^dUsing TCSPC and multiexponential analysis unless stated otherwise. Also note that no measurement of the fluorescence quantum yield is possible at this temperature since the method requires a special cell to measure the absorbance with accuracy.

^eUsing a streak camera as the fluorescence intensity is too weak.

^fThe instrument response function (IRF) of the fs laser/streak camera setup is ~ 8.0 ps, so these τ_{F} values should be taken as ≤ 8 ps.

^gNot investigated.

^hThe decay, residuals, best fit, and IRF profiles are provided in Figure S20.

P2 exhibits a multiexponential fluorescence decay at 77 K (four components are extracted at best fit), which is consistent with that observed for the models **2a**, **2b**, **M1**, and **M2** (triple exponential fluorescence decays are noted). This behavior may speculatively stem from various conformations adopted by the BMPA groups with respect to the anthraquinone diimine central core. This hypothesis is supported by the 298 K data where only one lifetime is observed. The τ_F datum for **P1** at 77 K is only ≤ 8 ps (limit of the IRF) compared to those for **P2** (0.18 (5), 0.80 (5), 3.7 (36), 10.6 ns (54%); Figure S20). Attempts to explain this drastic difference from DFT and TDDFT calculations described above failed as no significant differences were found. Because **P1** ($\tau_F \leq 8$ ps) and **P2** ($\tau_F = 10$ ps) in 2MeTHF exhibit S_1 lifetimes near the IRF of the streak camera (~ 8 ps), these values were checked against those extracted from fs-transient absorption spectroscopy (fs-TAS; Table 4 and Figure 7). Indeed, using $\lambda_{exc} = 475$ nm, three components are depicted after deconvolution of the time-resolved spectra (see data in the frames). These lifetimes are associated with the three singlet excited states that are formed when exciting at 475 nm ($S_0 \rightarrow S_1$, $S_0 \rightarrow S_2$, and $S_0 \rightarrow S_3$; see Table 3 and Figure 6 for details), presumably relaxing at ~ 10 , ~ 0.5 , and ~ 0.1 ps, respectively. Importantly, the 9.91 (**P1**) and 10.4 ps (**P2**) values match those obtained with the streak camera when taking into account the uncertainties. Finally, neither **P1** nor **P2** exhibits any emission as thin films at 298 K.

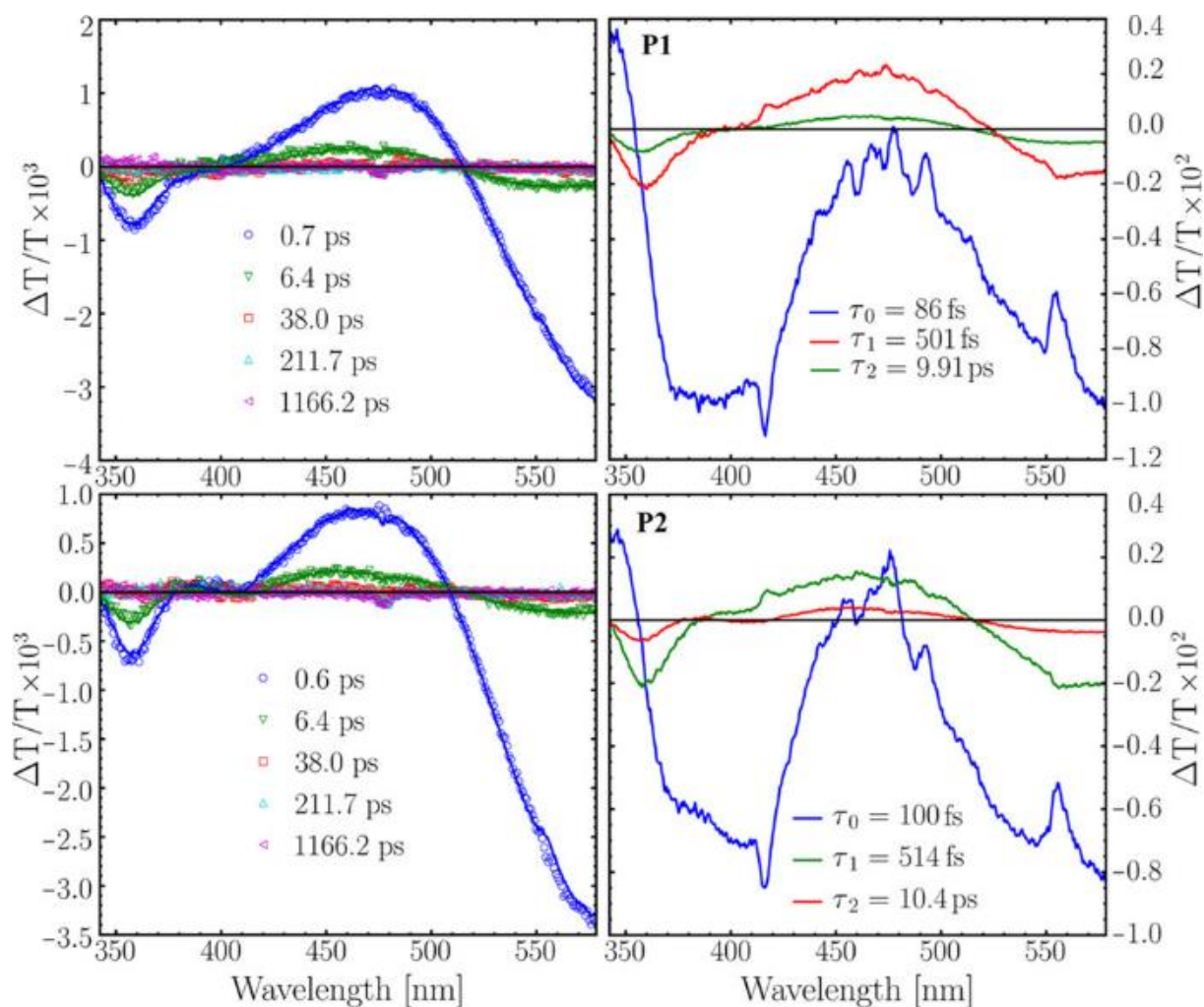


Figure 7. Left: evolution of the fs-TAS of **P1** (top) and **P2** (bottom) in 2MeTHF. Note that the positive and negative responses represent, respectively, the bleached and transient signals. IRF being, respectively, 138 and 148 fs ($\lambda_{\text{exc}} = 475$ nm) for **P1** and **P2**, the short components (86 and 100 fs) should be equal to or less than these IRF values. Right: decay-associated spectra of **P1** and **P2**. The uncertainties are ± 5 –10% based on multiple measurements. T is the transmittance.

Phosphorescence Spectra and Triplet States

To propose an explanation for the large discrepancy in τ_{F} behavior between **P1** and **P2** at 77 K, the triplet emission of the [**Pt**] moiety was also examined. Note that no emission over 800 nm was detected using a near-IR detector extending to 1380 nm. So the triplet emission (T_1) associated with the fluorescent CT excited state (S_1) was not observed. Concurrently, the upper energy triplet emission of the [**Pt**] units was detected for both **P1** (moderate relative intensity) and **P2** (very weak). The general shape of the emission bands is reminiscent of what is reported

in the literature for this type of motif (Figure 8), (46,47) but notable differences are depicted for their corresponding emission lifetimes (τ_p ; Table 5).

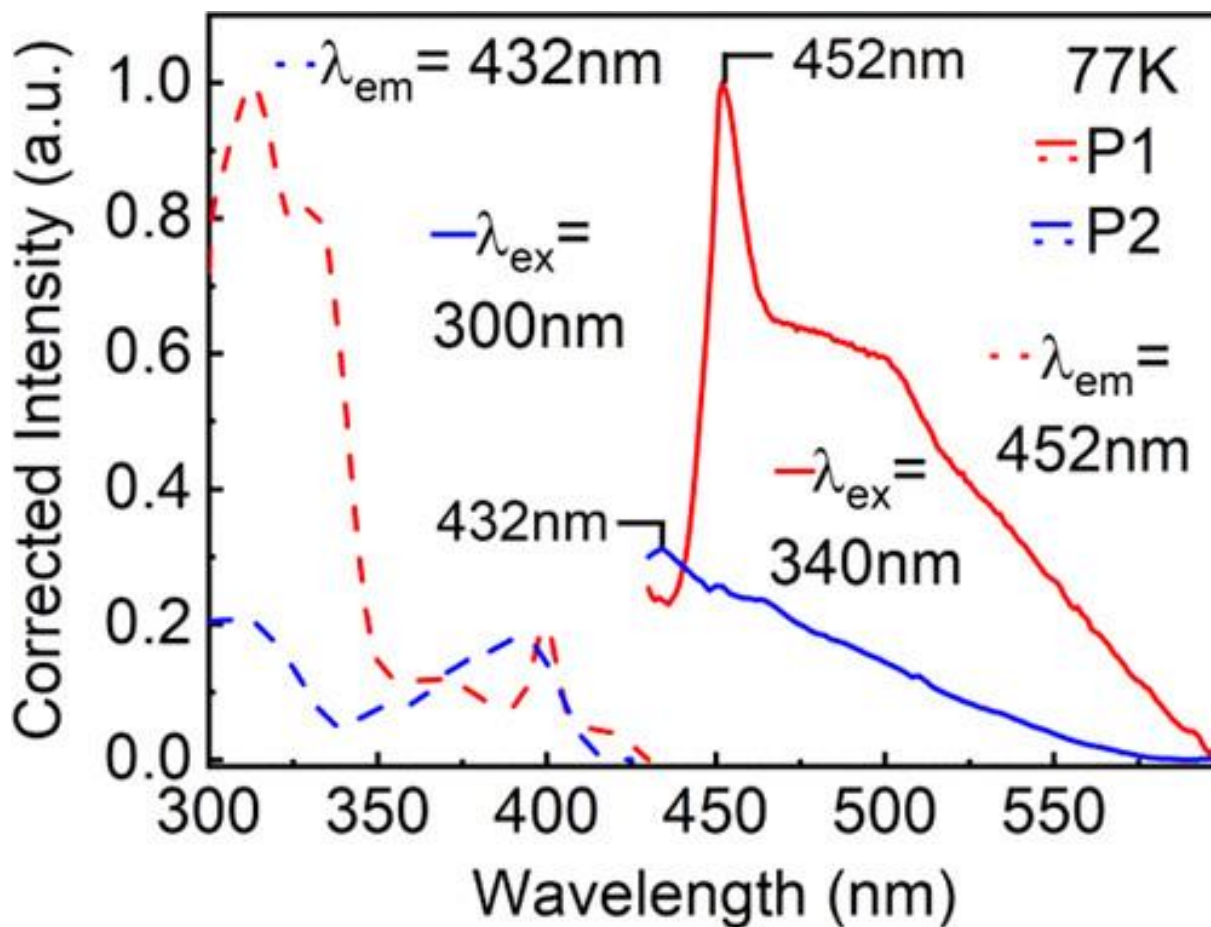


Figure 8. Emission (straight line) and excitation (broken line) spectra of **P1** (red) and **P2** (blue) in 2MeTHF at 77 K. Note that the relative intensity of the **P2** bands is very weak.

Table 5. Comparison of the τ_p Data for P1–5 in 2MeTHF at 77 K

	ref	chromophore	τ_p (relative contribution, %) (in μs) ^a	
P1	this work	[Pt]	1.46 (51), 61.8 (49) ^a	$\chi^2 = 1.026$
P2	this work	[Pt]	0.0011 (22), 0.0044 (36), 0.017 (42) ^b	$\chi^2 = 1.040$
P3	(14)	[Pt]	33.4 (55), 76.2 (45)	
P4	(14)	[Pt]	46.3, ^c 75.6 ^c	
P5	(14)	[Pt]	33.2, ^c 60.3 ^c	

^aThe uncertainties are $\pm 5\%$ (TCSPC).

^bThe uncertainties are $\pm 10\%$ based on multiple measurements and using TCSPC and multiexponential analysis. The IRF = 90 ps for these measurements using a diode laser ($\lambda_{\text{exc}} = 365$ nm).

^cThe χ^2 and the relative contribution (in %) were not provided in these cases.

The presence of biexponential emission decays for **P1** is not unprecedented (see data for **P3–5**). It was interpreted as a possible presence of multiple conformers. This hypothesis was unambiguously demonstrated afterward in a recent detailed analysis for model complexes in both the solid state and in frozen solution at 77 K. (77,78) For **P1**, two components are observed, but the shorter one (1.46 μs) is unusually small, whereas the longer one (61.8 μs) compares favorably with those for **P3–5**: 60–76 μs . (46,47) This large difference (i.e., by ~ 2 orders of magnitude) cannot be comfortably assigned to the presence conformers although they must be present. The τ_{P} data for **P2** shines some light on a possible explanation as its time scale is unusually and unexpectedly short (1.1, 4.4, and 17 ns). This amplitude is also consistent with the rather low intensity of the corresponding emission spectrum of the **[Pt]** moiety. Based on the facts that for **P2**, $X = X' = \text{BMPA}$ and τ_{P} is very short, and for **P3**, $X = X' = \text{H}$ and the τ_{P} values are longer (33 and 76 μs), the qualitative structure–property relationship may be related to a preference (or a dominance) in electronic communication across the conjugated systems as illustrated in Figure 9. If $X = \text{H}$ (see green conjugation), τ_{P} is large. If $X' = \text{BMPA}$ (see blue conjugation), τ_{P} is short. Evidence for conjugation going from BMPA and extending to **[Pt]** is also provided by the illustrations of the frontier MOs (Figures 4 and 5). So, **P1** appears as an intermediate case between **P2**, and **P3** and **P4**, both in structure and in fluorescence lifetimes.

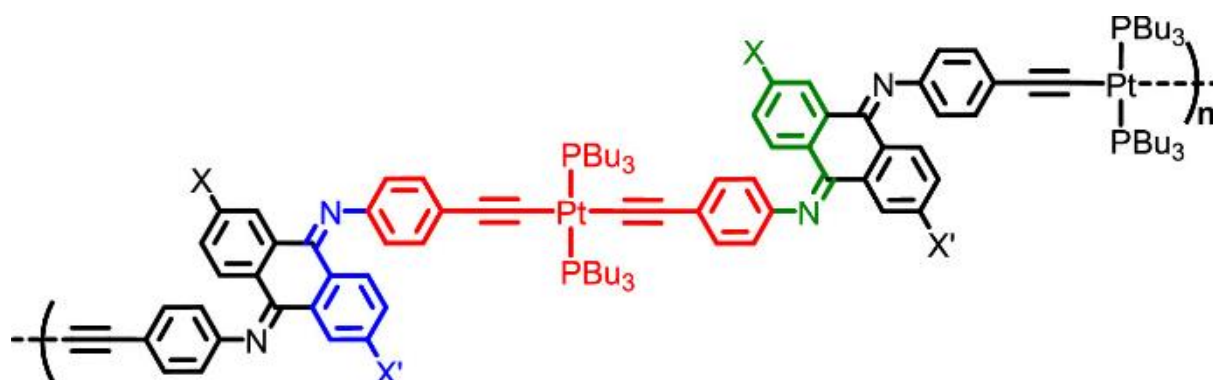


Figure 9. Structure of a segment of **P1** ($X = \text{H}$; $X' = \text{BMPA}$) stressing the difference in X and X' with respect to conjugation with the $\text{C}\equiv\text{C}\text{PtC}\equiv\text{C}$ moiety as a possible explanation of the unexpectedly large difference in τ_{P} 's in its biexponential emission decays of the **[Pt]** unit.

Again, no emission of the T_1 states was observed. However, evidence for their presence was obtained from the fs-TAS in the solid state (as films) as the delay line reached 8 ns (Figure 10). For **P1**, the three fs-ps components are again observed (“83” fs, 678 fs, and 21.1 ps), but for **M1**, only two species (201 fs and 9.97 ps) are noted, which is in fact in agreement with the computed predictions of Table 3 (and Figure 6) for **M1** when exciting at 470 nm (here $S_0 \rightarrow S_1$, $S_0 \rightarrow S_2$). The longest lifetimes, here $\tau(S_1)$, of **M1** (9.97 ps) and **P1** (21.1 ps), are in the same order of magnitude of the data measured in 2MeTHF solution (i.e., 9.3 ps (streak) and 9.91 ps (fs-TAS)). However, both **M1** and **P1** exhibit supplementary species decaying in the ns time scale. These species are unambiguously triplet state species, and the very short lifetimes (short ns) are far from what is generally expected for a [Pt]-containing chromophore (μ s), and explain the absence of phosphorescence arising from the T_1 state. Clearly, very short-lived excited states, singlet and triplet, are common for this type of materials. This exhaustive photophysical characterization of these new materials indicates that to observe any efficient photoinduced electron transfer from the singlet states, these rates must be ultrafast, i.e., fs or short ps time scale.

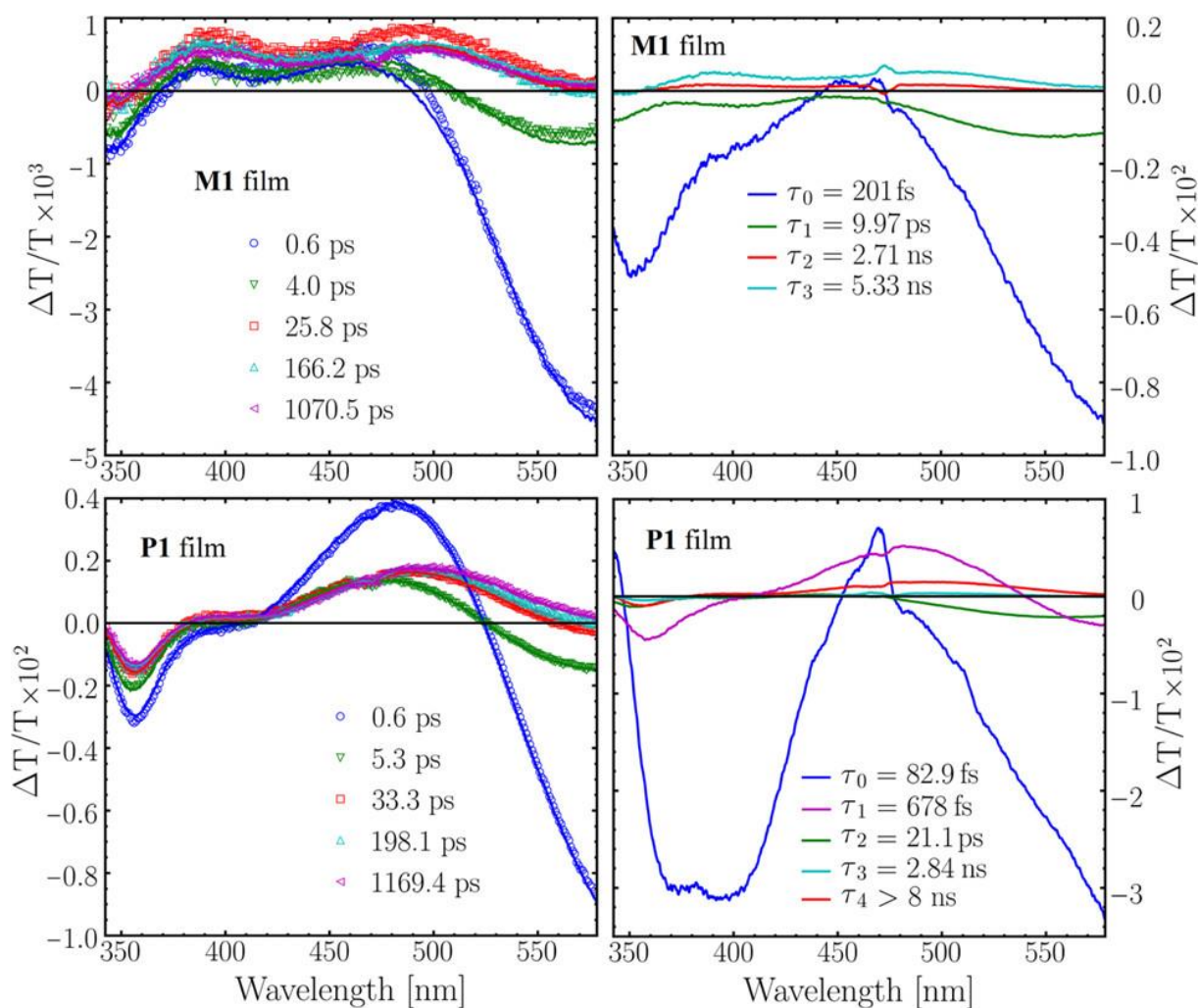


Figure 10. Left: evolution of the fs-TAS of **M1** (top) and **P1** (bottom) as films. Note that the positive and negative responses represent, respectively, the bleached and transient signals. IRF being, respectively, 134 and 157 fs ($\lambda_{\text{exc}} = 475$ nm) for **M1** and **P1**, the short components (~ 83 fs) should be equal to or less than the IRF value of 157 fs. Right: decay-associated spectra of **M1** and **P1**. The uncertainties are $\pm 5\text{--}10\%$ based on multiple measurements. T is the transmittance.

Photoinduced Electron Transfer to PCBM in 2MeTHF Solution

The presence of an intense fluorescence for **P2** at 77 K permits an investigation on the intermolecular photoinduced electron transfer. Here, PCBM is employed as an electron acceptor (79–81) for the specific study of the potential oxidative (eq 1) (79) or reductive (eq 2) (80,81) quenching process



The (**[Pt]**-**[AQI]**)_{*n*} (and (**[Pt]**-**[QI]**)_{*n*}) polymers exhibit invariably a 1-electron oxidation step at $\sim +1.1$ V versus saturated calomel electrode (SCE) (45–53) as this process is mainly centered onto the **[Pt]** unit (the sampling is about 12 polymers from the literature). Using the absorption spectra (Figure 1), the origin of the electronic transition is ~ 575 nm (~ 2.16 eV) for **P1*** and **P2***. By using +1.1 V versus SCE for the oxidation potentials of **P1** and **P2**, the driving force for photo-oxidative electron transfer ($\mathbf{Px}^* \rightarrow \mathbf{Px}^{+\bullet} + 1e^-$; $x = 1, 2$) is estimated as $2.16 - 1.1 \approx +1.06$ V versus SCE. Concurrently, PCBM is reduced at -0.94 V versus SCE (note that this potential has been converted from vs Ag/Ag⁺ into vs SCE as the reference electrode). (82) The potential difference, ΔE , for eq 1 can be evaluated from $+1.06 - 0.94 \approx 0.12$ V versus SCE. For eq 2, using the position of the fluorescence band (~ 705 nm; ~ 1.76 eV), the driving force for the photoreductive electron transfer ($\text{PCBM}^* + 1e^- \rightarrow \text{PCBM}^{\bullet-}$) is given by $-0.94 + 1.76 \approx +0.82$ V versus SCE. So, the ΔE value of eq 2 can be evaluated from $+0.82 - 1.1 \approx -0.27$ V versus SCE. Consequently, eqs 1 and 2 have, respectively, positive and negative potential differences of $\sim +0.12$ and ~ -0.27 V versus SCE. Reaction 2 is not thermodynamically favorable. (83) The modified Latimer diagrams are shown in Figure S21.

PCBM is fluorescent (Figure S22), in agreement with the literature. (84,85) The spectral evolution of the fluorescence spectrum of **P2** at constant concentration in a 2MeTHF glass at 77 K upon additions of PCBM (note that $\lambda_{\text{exc}} = 460$ nm, both **P2** and PCBM are excited) shows

a decrease in **P2** fluorescence intensity since **P2**⁺ is nonemissive (Figure 11). Part of this decrease is due to the expected inner-filtering effect ($\epsilon(\text{PCBM}) = 700 \text{ M}^{-1} \text{ cm}^{-1}$, 460 nm, 77 K), but the decrease is more pronounced than anticipated. More strikingly, the 4-fold expected increase in the fluorescence intensity of PCBM with its concentration is much less than anticipated, even when considering inner filtering, indicating quenching (note: PCBM⁻ is nonemissive).

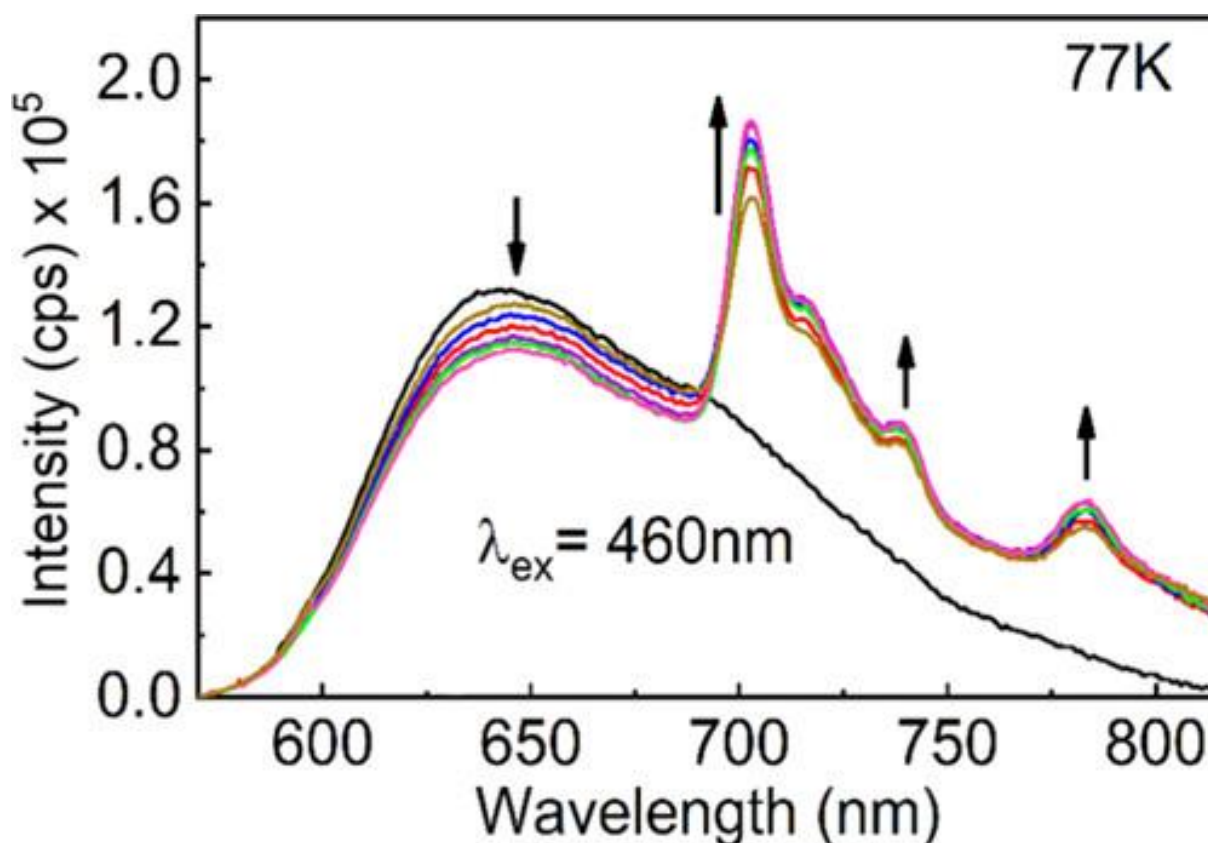


Figure 11. Evolution of fluorescence spectra of **P2** ($3.1 \times 10^{-4} \text{ M}$ based on one unit and kept constant) at 77 K upon successive additions of PCBM: 0 (black), 9.22×10^{-5} (brown), 1.54×10^{-4} (red), 2.15×10^{-4} (blue), 2.77×10^{-4} (purple), 3.88×10^{-4} (green), and $3.996 \times 10^{-4} \text{ M}$ (pink). $\lambda_{\text{exc}} = 460 \text{ nm}$. The absorption, excitation, and fluorescence spectra of PCBM in 2MeTHF at 77 K are shown in Figure S22.

In statically distributed donors and acceptors in a given volume, one must consider the fact that some donor...acceptor dyads are placed outside and within the sphere of quenching. (83) Consequently, a fraction of the excited species will be unquenched and another part will be quenched with a gradient with the statistical distance distribution. (83) This static quenching was monitored using their τ_{F} 's (i.e., **P2** alone, Table 4; PCBM alone, **P2/PCBM**, Table 6). PCBM exhibits a τ_{F} value of 1.65 ns at 77 K, also consistent with

the literature. (84) When mixed with **P2** and monitored at 720 nm (where PCBM emits), an unquenched component of 1.52 ns (the uncertainties are $\pm 5\%$ based on multiple measurements) is depicted. The absence of detectable quenching for this component (PCBM*) is consistent with the fact that photoinduced reductive quenching of PCBM* is thermodynamically unfavorable (eq 2).

Table 6. τ_F Data of PCBM and P2 + PCBM at 77 K in 2MeTHF^a

	λ (nm)	τ_F^b (ns)	assignment	χ^2 ^b
PCBM	720	1.65 (100%)	PCBM	1.022
P2 + PCBM	640	0.35 (2%) ^c	P2	1.041
		2.72 (45%)	P2	
		6.18 (53%)	P2	
P2 + PCBM	720	1.52 (33%)	PCBM	1.049
		3.05 (42%)	P2	
		6.45 (25%)	P2	

^a $[\text{PCBM}] = 1.02 \times 10^{-4}$ M. $[\text{P2}] = 8.7 \times 10^{-6}$ M (based on one unit). Using TCSPC and multiexponential analysis.

^b The values are extracted from multiexponential analyses.

^c With 2% of relative intensity, the accuracy on the extracted τ_F is uncertain.

Concurrently, two components associated with **P2** are also noted at 640 nm where **P2** does emit and at 720 nm where both **P2** and PCBM emit. The τ_F values in the **P2**/PCBM mixtures (2.7 (45%) and 6.2 (53%) ns) are shorter than that noted for **P2** alone ($\tau_F = 3.7$ (36%) and 10.6 (54%) ns; Table 4; the difference between 10.6 (unquenched) and 6.2 ns (quenched) is significant), thus supporting evidence for a photo-oxidative quenching: $\text{P2}^* + \text{PCBM} \rightarrow \text{P2}^{+*} + \text{PCBM}^-$.

Because of the statistical distribution of the **P2**...PCBM separations in frozen media and the fact that for electron transfer, k_{et} is distance dependent, the application of the exponential series method (ESM) (55,56) is more appropriate for the analysis of the fluorescence decays and was also applied. Indeed, this method permits one to compute a large number of components in the emission decays (here up to 200) and to report their relative contribution versus lifetimes. This graph translates in a distribution of τ_F 's, as indeed observed for the **P2**/PCBM mixtures (Figure 12). As blank experiments, the same ESM analysis was performed for PCBM alone and **P2** alone, and only narrow distributions were observed (see Figures S23 and S24).

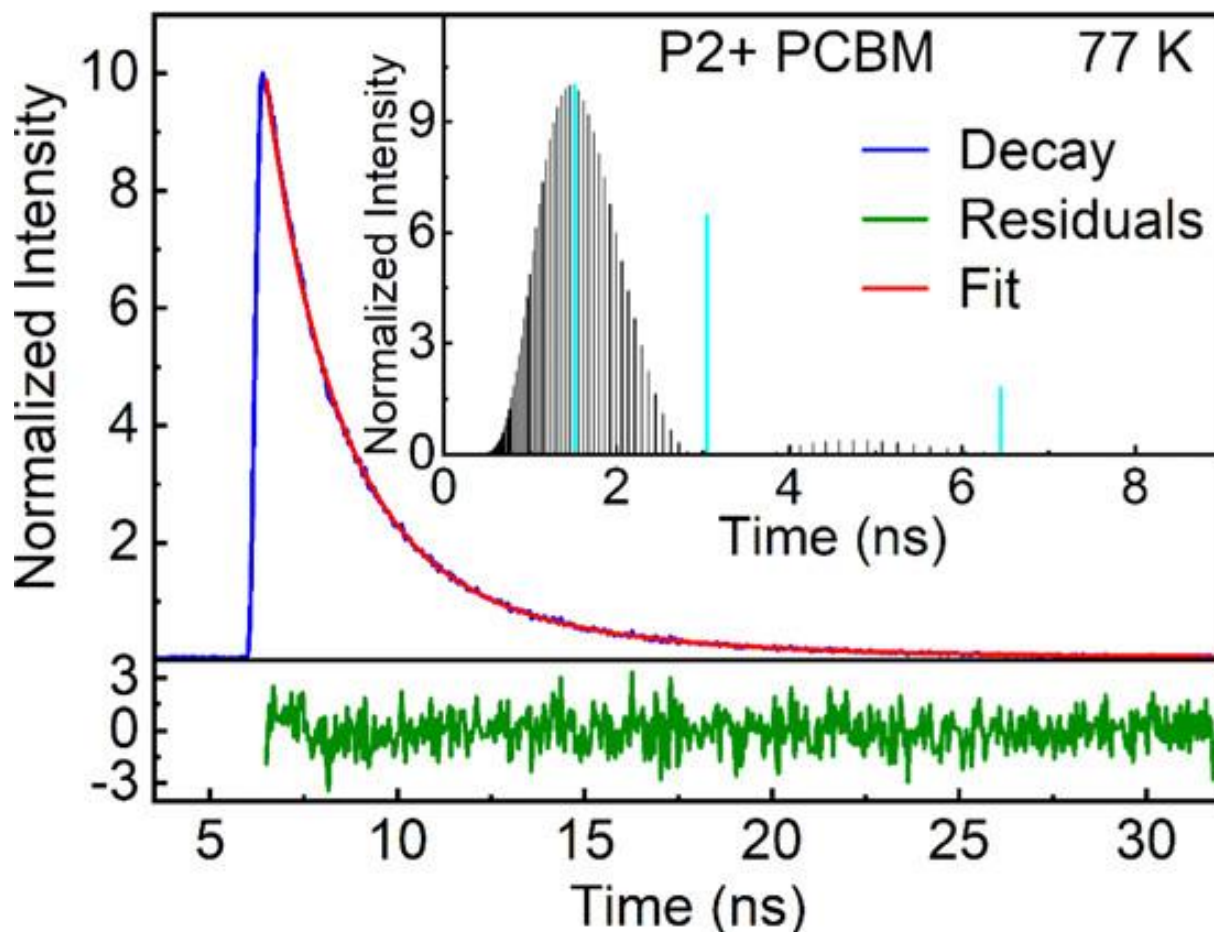


Figure 12. Emission decay (blue), residuals (green), and best fit (red) of **P2** in 2MeTHF at 77 K. Multiexponential analysis yields $\tau_e = 1.52$ (33%), 3.05 (42%), and 6.45 (25%) ns; $\chi^2 = 1.049$. $[\text{PCBM}] = 1.02 \times 10^{-4}$ M. $[\text{P2}] = 8.7 \times 10^{-6}$ M (based on one unit). Inset: multiexponential analysis (sky blue) and ESM analysis (black). $\lambda_{\text{exc}} = 443$ nm, $\lambda_{\text{em}} = 720$ nm. See Figures S22 and S23 for **P2** alone and PCBM alone at 77 K. In this figure, the multiexponential analysis results are compared to those for ESM.

Photoinduced Electron Transfer of P1 and P2 to PCBM in Films

Because PCBM is also emissive in the solid state, one can also use this analytical signal to address the electron transfer process in films taking advantage that the electron donor and acceptor are always at minimal proximity. Indeed, despite the absence of fluorescence for both **P1** and **P2**, evidence for electron transfer is provided (Figure 13). In the absence of **P1** or **P2**, the PCBM film exhibits a structureless fluorescence band that matches that reported in the literature. (85) The τ_F value for PCBM is 0.44 ± 0.01 ns ($\chi^2 = 1.09$; Figure S24). In a 1:1 relative ratio, complete quenching of the PCBM fluorescence is indeed observed for

both **P1** and **P2**, which is fully consistent with the formation of the nonemissive PCBM⁻ species.

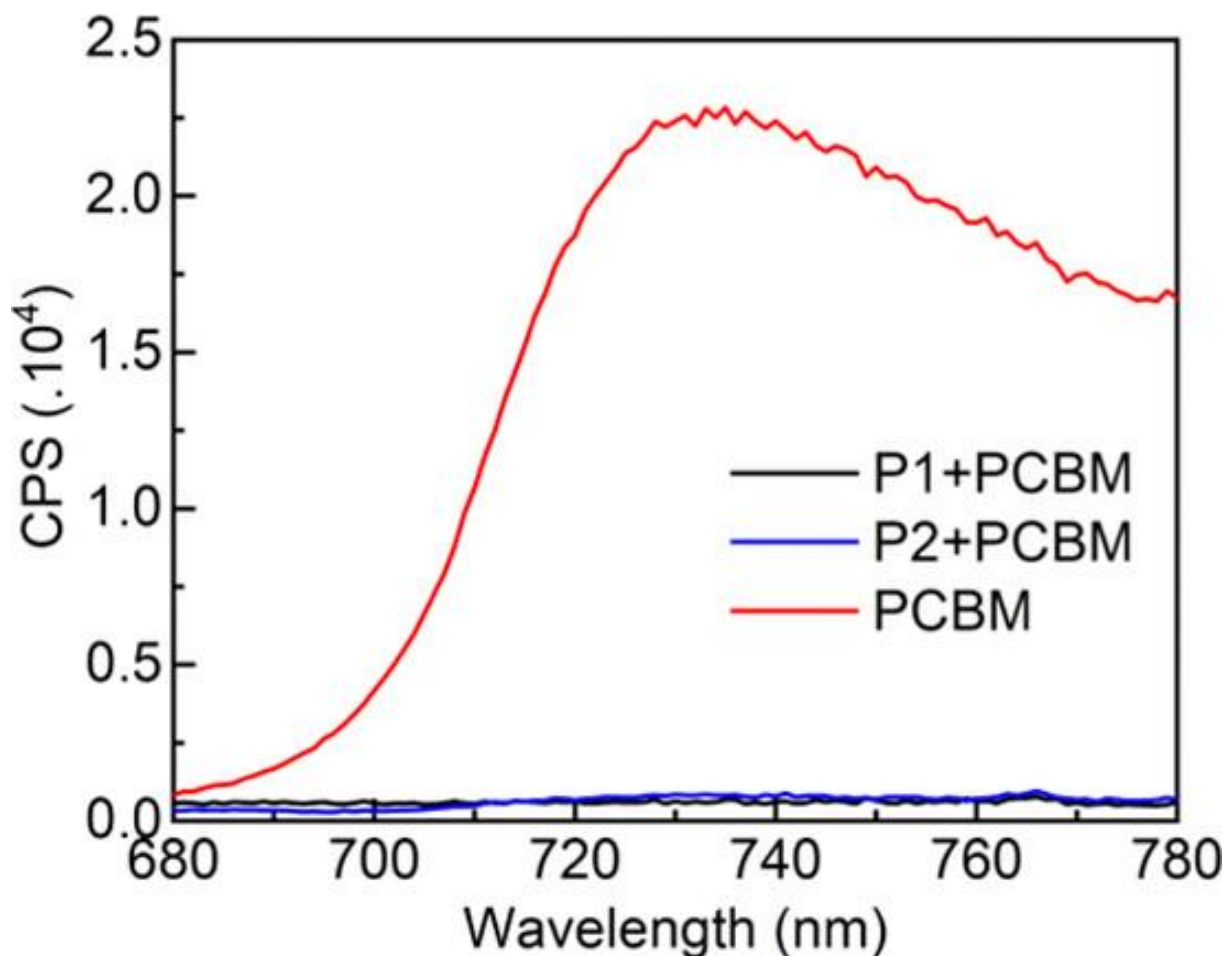


Figure 13. Fluorescence spectra of PCBM (red), **P1**/PCBM (black), and **P2**/PCBM (blue) mixtures (in 1:1 relative amount based on one unit of polymer) as a film at 298 K ($\lambda_{\text{exc}} = 460$ nm). The absorption spectra of these films are provided in Figure S25.

Noteworthy, the ratio 1:1 polymer/PCBM is selected in this kinetic study because the literature shows that the best PCE values are generally near this relative quantity. (86,87) Noteworthy, this experiment also demonstrates that this quenching process is not due to a singlet energy transfer. This conclusion stems from the fact that in such a case, the energy donor and acceptor would be the polymers and PCBM, respectively, based on the position of their fluorescence bands (Figure 11). Upon energy transfer, the donor fluorescence is quenched, but not that for the acceptor. This is clearly not the case as the PCBM fluorescence is completely quenched in the polymer/PCBM films. The time scale of this process has been examined by fs-TAS of the films (Figure 14; the absorption spectra of the films are shown in Figure S25). The neat film of PCBM exhibits a transient at 460 nm (that remained in the negative) and two bleached signals

at 380 and 565 nm (Figure 14, top). After deconvolution, four species are depicted. One is decaying with a time constant of 437 ps and is the S_1 state species deduced from τ_F mentioned above. Moreover, a charge separation can also occur in neat films of PCBM (called Frenkel exciton; $PCBM^* + PCBM \rightarrow PCBM^{+\bullet} + PCBM^{-\bullet}$) and fullerene, (88,89) and the charge recombination can occur in the ns time scale. The $PCBM^{+\bullet}$ component is indeed observed as a broader signal decaying with a time constant of ~ 7.8 ns (Figure 13, top right, turquoise line). This broad component is also depicted in the decay-associated spectra for the **P1**/PCBM and **P2**/PCBM films (see turquoise and purple lines in Figure 14, middle and bottom right), also decaying in the ns time scale (≥ 8 and 2.06 ns).

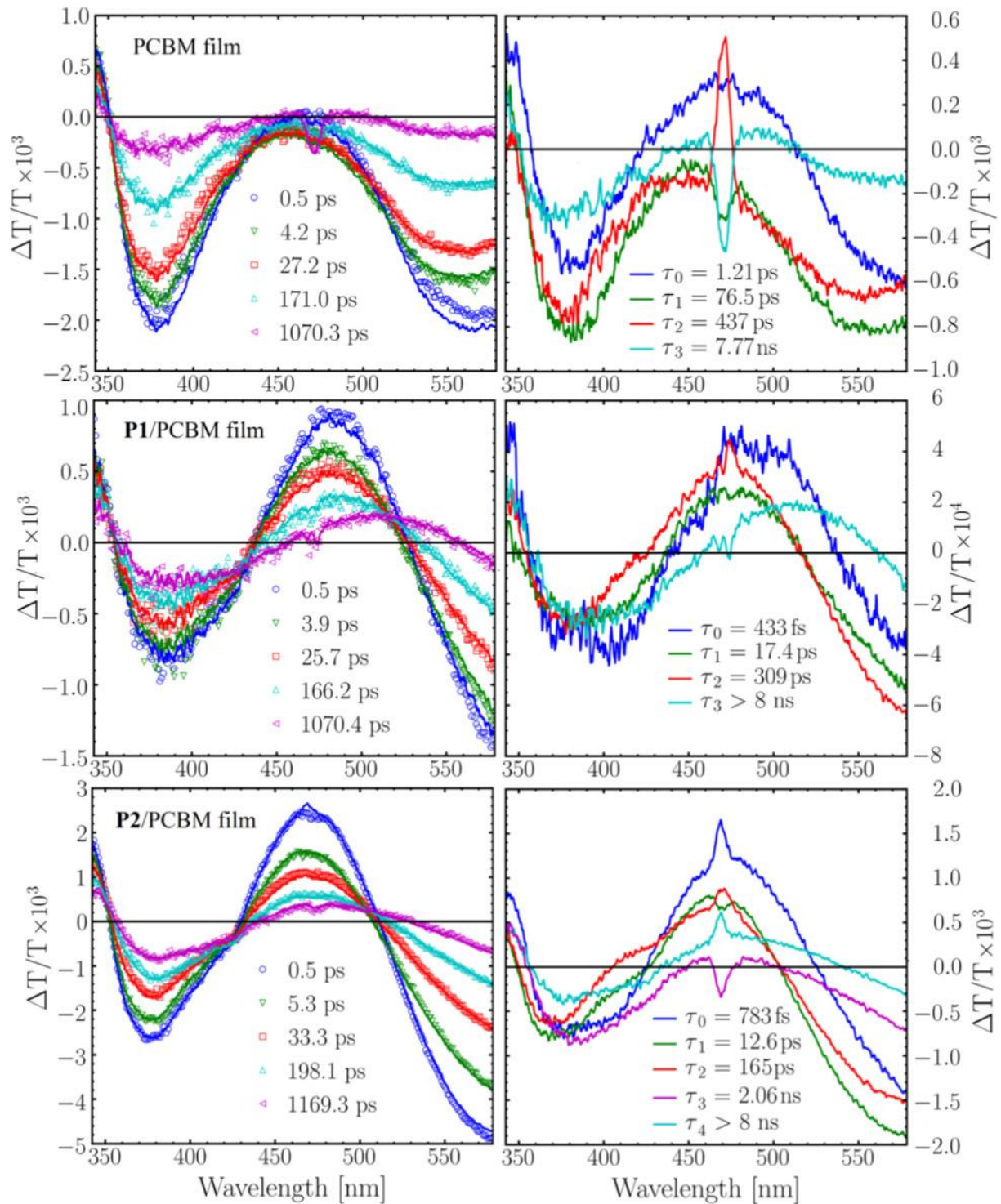


Figure 14. Left: evolution of the fs-TAS of **PCBM** (top), 1:1 **P1/PCBM** (middle), and 1:1 **P2/PCBM** (bottom) films ($\lambda_{\text{exc}} = 470$ nm). The IRF values are respectively, 152, 127, and 141 fs. Note that the positive and negative responses represent the bleached and transient signals, respectively. Right: decay-associated spectra of **M1** and **P1**. The uncertainties on the lifetimes are ± 5 – 10% based on multiple measurements. T is the transmittance. The fs-TAS spectra in the 850–1100 nm range are shown in Figures S26 and S27.

However, the fs-TAS responses of **P1** and **P2** versus that of PCBM (Figures 7, 10, and 14) are very similar. This situation prevents one from assigning each individual component with certainty. Nonetheless in all cases, the transient species are formed within the laser pulse with no rise time exceeding the IRF (127–141 fs) meaning that the rate for electron transfer, $k_{\text{et}} \geq 6.6 \times 10^{12} \text{ s}^{-1}$. This conclusion is fully consistent with the experimentally determined k_{et} values reported for other related PCBM-containing molecular models and blends, (90–92) although somewhat slower rates have also been reported (with time scales ranging from 360 to 420 fs), (93,94) and is also consistent with the conclusion drawn above that in the case of an oxidative quenching ($\text{P}\mathbf{x}^* + \text{PCBM} \rightarrow \text{P}\mathbf{x}^{+\bullet} + \text{PCBM}^{-\bullet}$), the k_{et} values must be very large to overcome the rather short-lived S_1 state of **P1** and **P2**, which are in the order of 10 ps (i.e., $\tau(\text{S}_1) \leq 8\text{--}21$ ps, at 298 K, in solution and as films).

Conclusions

From the spectroscopic and photophysical standpoints, the anchoring of the BMPA groups turned out beneficial since fluorescence arising from the lowest energy excited state, S_1 (described as a CT state; $[\text{Pt}] \rightarrow \text{AQI}$ (major component) and $\text{BMPA} \rightarrow \text{AQI}$ (minor component)), was observed for the first time for this type of push–pull materials, namely, $([\text{Pt}]-(\text{AQI}))_n$ and $([\text{Pt}]-(\text{AQ}))_n$. Thus, this signal then permitted one to monitor the photoinduced electron transfer from the electron-donor polymer, namely, **P2**, to the acceptor PCBM in solution. The DFT computational data on **P1** and **P2** indicated that the atomic contributions of the HOMO were significantly larger on $[\text{Pt}]$, which then suggest that this moiety represents the electron-donor segment of the polymers during the electron transfer. This conclusion is unprecedented and could explain the large number of literature works using this synthon for the construction of solar cells. (23–34) Using 1:1 polymer/PCBM films, fs-TAS established that the k_{et} values are ultrafast (time scale ≤ 150 fs; IRF limit).

Supporting Information

Computed positions and oscillator strength for the 100 electronic transitions; calculated positions of the pure electronic transitions, oscillator strengths, and major contributions; ^1H NMR, ^{31}P NMR, and MALDI-TOF spectra; emission spectrum of **2b** in 2MeTHF at 298 K in the near-IR region and fluorescence spectrum and decay of PCBM in 2MeTHF at 77 K

Author Information

Corresponding Author

- **Pierre D. Harvey** - *Département de chimie, Université de Sherbrooke, Sherbrooke, PQ, Canada JIK 2R1*; <http://orcid.org/0000-0002-6809-1629>; Email: Pierre.Harvey@USherbrooke.ca

Authors

- **Frank Juvenal** - *Département de chimie, Université de Sherbrooke, Sherbrooke, PQ, Canada JIK 2R1*; <http://orcid.org/0000-0001-6471-0755>
- **Hu Lei** - *Département de chimie, Université de Sherbrooke, Sherbrooke, PQ, Canada JIK 2R1*
- **Adrien Schlachter** - *Département de chimie, Université de Sherbrooke, Sherbrooke, PQ, Canada JIK 2R1*; <http://orcid.org/0000-0001-5215-8908>
- **Paul-Ludovic Karsenti** - *Département de chimie, Université de Sherbrooke, Sherbrooke, PQ, Canada JIK 2R1*

Notes

The authors declare no competing financial interest.

Acknowledgments

The NSERC, Natural Sciences and Engineering Research Council of Canada, the FRQNT, Fonds de Recherche du Québec—Nature et Technologies, the CQMF, Centre Québécois des Matériaux Fonctionnels, and the CEMAPUS, Centre d'Études des Matériaux Avancés et Photoniques de l'Université de Sherbrooke, are thanked for their financial support.

References

1. Gauthier, S.; Porter, A.; Achelle, S.; Roisnel, T.; Dorcet, V.; Barsella, A.; Le Poul, N.; Level, P. G.; Jacquemin, D.; Robin-Le Guen, F. Mono- and Diplatinum Polyynediyl Complexes as Potential Push-Pull Chromophores: Synthesis, Characterization, TD-DFT Modeling, and Photophysical and NLO Properties. *Organometallics* **2018**, *37*, 2232–2244, DOI: 10.1021/acs.organomet.8b00223
2. Durand, R. J.; Gauthier, S.; Achelle, S.; Kahlal, S.; Saillard, J.-Y.; Barsella, A.; Wojcik, L.; Le Poul, N.; Robin-Le Guen, F. Incorporation of a Platinum Center in the Pi-Conjugated

Core of Push-Pull Chromophores for Nonlinear Optics (NLO). *Dalton Trans.* **2017**, *46*, 3059– 3069, DOI: 10.1039/C7DT00252A

3. Colombo, A.; Nisic, F.; Dragonetti, C.; Marinotto, D.; Oliveri, I. P.; Righetto, S.; Lobello, M. G.; De Angelis, F. Unexpectedly High Second-Order Nonlinear Optical Properties of Simple Ru and Pt Alkynyl Complexes as an Analytical Springboard for NLO-Active Polymer Films. *Chem. Commun.* **2014**, *50*, 7986– 7989, DOI: 10.1039/c4cc02432j
4. Kindahl, T.; Ohgren, J.; Lopes, C.; Eliasson, B. Synthesis, Optical Power Limiting, and DFT Calculations of Triplet-Triplet Absorption of Three Novel Pt(II)-Diacetylide Chromophores. *Tetrahedron Lett.* **2013**, *54*, 2403– 2408, DOI: 10.1016/j.tetlet.2013.02.105
5. Maiti, S. K.; Jardim, M. G.; Rodrigues, J.; Rissanen, K.; Campo, J.; Wenseleers, W. Divergent Route to the Preparation of Hybrid Pt-Fe 2,4,6-Tris(4-ethynylphenyl)-1,3,5-triazine Metallodendrimers for Nonlinear Optics. *Organometallics* **2013**, *32*, 406– 414, DOI: 10.1021/om300745v
6. Dubinina, G. G.; Price, R. S.; Abboud, K. A.; Wicks, G.; Wnuk, P.; Stepanenko, Y.; Drobizhev, M.; Rebane, A.; Schanze, K. S. Phenylene Vinylene Platinum(II) Acetylides with Prodigious Two-Photon Absorption. *J. Am. Chem. Soc.* **2012**, *134*, 19346– 19349, DOI: 10.1021/ja309393c
7. Kindahl, T.; Ellingsen, P. G.; Lopes, C.; Braennlund, C.; Lindgren, M.; Eliasson, B. Photophysical and DFT Characterization of Novel Pt(II)-Coupled 2,5-Diaryloxazoles for Nonlinear Optical Absorption. *J. Phys. Chem. A.* **2012**, *116*, 11519– 11530, DOI: 10.1021/jp307312v
8. Chan, C. K. M.; Tao, C.-H.; Li, K.-F.; Wong, K. M.-C.; Zhu, N.; Cheah, K.-W.; Yam, V. W.-W. Design, Synthesis, Characterization, Luminescence and Non-Linear Optical (NLO) Properties of Multinuclear Platinum(II) Alkynyl Complexes. *Dalton Trans.* **2011**, *40*, 10670– 10685, DOI: 10.1039/c1dt10784d
9. Chan, C. K.-M.; Tao, C.-H.; Li, K.-F.; Wong, K. M.-C.; Zhu, N.-Y.; Cheah, K.-W.; Yam, V. W.-W. Synthesis, Characterization, Luminescence and Nonlinear Optical (NLO) Properties of Truxene-Containing Platinum(II) Alkynyl Complexes. *J. Organomet. Chem.* **2011**, *696*, 1163– 1173, DOI: 10.1016/j.jorganchem.2010.09.044

10. Vestberg, R.; Westlund, R.; Eriksson, A.; Lopes, C.; Carlsson, M.; Eliasson, B.; Glimsdal, E.; Lindgren, M.; Malmstroem, E. Dendron Decorated Platinum(II) Acetylides for Optical Power Limiting. *Macromolecules* **2006**, *39*, 2238– 2246, DOI: 10.1021/ma0523670
11. D'Amato, R.; Furlani, A.; Colapietro, M.; Portalone, G.; Casalbani, M.; Falconieri, M.; Russo, M. V. Synthesis, Characterisation and Optical Properties of Symmetrical and Unsymmetrical Pt(II) and Pd(II) Bis-Acetylides. Crystal Structure of *trans*-[Pt(PPh₃)₂(C≡C-C₆H₅)(C≡C-C₆H₄NO₂)]. *J. Organomet. Chem.* **2001**, *627*, 13– 22, DOI: 10.1016/S0022-328X(00)00791-9
12. Siemsen, P.; Gubler, U.; Bosshard, C.; Gunter, P.; Diederich, F. Pt-Tetraethynylethene Molecular Scaffolding: Synthesis and Characterization of a Novel Class of Organometallic Molecular Rods. *Chem. – Eur. J.* **2001**, *7*, 1333– 1341, DOI: 10.1002/1521-3765(20010316)7:6<1333::AID-CHEM1333>3.0.CO;2-9
13. Shu, H.-X.; Wang, J.-Y.; Zhang, Q.-C.; Chen, Z.-N. Photophysical and Electro-luminescent Properties of PtAg₂ Acetylide Complexes Supported with meso- and rac-Tetraphosphine. *Inorg. Chem.* **2017**, *56*, 9461– 9473, DOI: 10.1021/acs.inorgchem.7b00452
14. Li, Y.-P.; Fan, X.-X.; Wu, Y.; Zeng, X.-C.; Wang, J.-Y.; Wei, Q.-H.; Chen, Z.-N. High-Efficiency Organic Light-Emitting Diodes of Phosphorescent PtAg₂heterotrinnuclear Acetylide Complexes Supported by Triphosphine. *J. Mater. Chem. C* **2017**, *5*, 3072– 3078, DOI: 10.1039/C7TC00382J
15. Zhang, L. Y.; Xu, L. J.; Wang, J. Y.; Zeng, X. C.; Chen, Z. N. Photoluminescence and Electroluminescence of Cationic PtAu₂heterotrinnuclear Complexes with Aromatic Acetylides. *Dalton Trans.* **2017**, *46*, 865– 874, DOI: 10.1039/C6DT04249J
16. Xu, L.-J.; Zeng, X.-C.; Wang, J.-Y.; Zhang, L.-Y.; Chi, Y.; Chen, Z.-N. Phosphorescent PtAu₂Complexes with Differently Positioned Carbazole-Acetylide Ligands for Solution-Processed Organic Light-Emitting Diodes with External Quantum Efficiencies of over 20%. *ACS Appl. Mater. Interfaces* **2016**, *8*, 20251– 20257, DOI: 10.1021/acsami.6b06707
17. Zeng, X.-C.; Wang, J.-Y.; Xu, L.-J.; Wen, H.-M.; Chen, Z.-N. Solution-Processed OLEDs Based on Phosphorescent PtAu₂complexes with Phenothiazine-Functionalized Acetylides. *J. Mater. Chem. C* **2016**, *4*, 6096– 6103, DOI: 10.1039/C6TC01539E

18. Jiménez, A. J.; Marcos, M. L.; Hausmann, A.; Rodríguez-Morgade, M. S.; Guldi, D. M.; Torres, T. Assembling Phthalocyanine Dimers through a Platinum(II) Acetylide Linker. *Chem. – Eur. J.* **2011**, *17*, 14139– 14146, DOI: 10.1002/chem.201101791
19. Goudreault, T.; He, Z.; Guo, Y.; Ho, C.-L.; Zhan, H.; Wang, Q.; Ho, K. Y.-F.; Wong, K.-L.; Fortin, D.; Yao, B. Synthesis, Light-Emitting, and Two-Photon Absorption Properties of Platinum-Containing Poly(arylene-ethynylene)s Linked by 1,3,4-Oxadiazole Units. *Macromolecules* **2010**, *43*, 7936– 7949, DOI: 10.1021/ma1009319
20. Ho, C.-L.; Chui, C.-H.; Wong, W.-Y.; Aly, S. M.; Fortin, D.; Harvey, P. D.; Yao, B.; Xie, Z.; Wang, L. Efficient Electrophosphorescence from a Platinum Metallopolyyne Featuring a 2,7-Carbazole Chromophore. *Macromol. Chem. Phys.* **2009**, *210*, 1786– 1798, DOI: 10.1002/macp.200900351
21. Guo, F.; Kim, Y.-G.; Reynolds, J. R.; Schanze, K. S. Platinum-Acetylide Polymer Based Solar Cells: Involvement of the Triplet State for Energy Conversion. *Chem. Commun.* **2006**, 1887– 1889, DOI: 10.1039/B516086C
22. Jiang, F.-L.; Fortin, D.; Harvey, P. D. Syntheses, Characterization, and Photophysical Properties of Conjugated Organometallic Pt-Acetylide/Zn(II) Porphyrin-Containing Oligomers. *Inorg. Chem.* **2010**, *49*, 2614– 2623, DOI: 10.1021/ic901421m
23. Siu, C.-H.; Lee, L. T. L.; Yiu, S.-C.; Ho, P.-Y.; Zhou, P.; Ho, C.-L.; Chen, T.; Liu, J.; Han, K.; Wong, W.-Y. Synthesis and Characterization of Phenothiazine-Based Platinum(II)-Acetylide Photosensitizers for Efficient Dye-Sensitized Solar Cells. *Chem. – Eur. J.* **2016**, *22*, 3750– 3757, DOI: 10.1002/chem.201503828
24. Wu, W.; Li, Z.-Y.; Zheng, Z.; Hu, Y.; Hua, J. π - π and p- π Conjugation, Which Is More Efficient for Intermolecular Charge Transfer in Starburst Triarylamine Donors of Platinum Acetylide Sensitizers?. *Dyes Pigm.* **2014**, *111*, 21– 29, DOI: 10.1016/j.dyepig.2014.04.017
25. Wu, W.; Xu, X.; Yang, H.; Hua, J.; Zhang, X.; Zhang, L.; Long, Y.; Tian, H. D- π -M- π -A Structured Platinum Acetylide Sensitizer for Dye-Sensitized Solar Cells. *J. Mater. Chem.* **2011**, *21*, 10666– 10671, DOI: 10.1039/c1jm10942a
26. Gauthier, S.; Caro, B.; Robin-Le Guen, F.; Bhuvanesh, N.; Gladysz, J. A.; Wojcik, L.; Le Poul, N.; Planchat, A.; Pellegrin, Y.; Blart, E. Synthesis, Photovoltaic Performances and TD-DFT Modeling of Push-Pull Diacetylide Platinum Complexes in TiO₂ based Dye-Sensitized Solar Cells. *Dalton Trans.* **2014**, *43*, 11233– 11242, DOI: 10.1039/C4DT00301B

27. Dai, F.-R.; Zhan, H.-M.; Liu, Q.; Fu, Y.-Y.; Li, J.-H.; Wang, Q.-W.; Xie, Z.; Wang, L.; Yan, F.; Wong, W.-Y. Platinum(II)-Bis(aryleneethynylene) Complexes for Solution-Processible Molecular Bulk Heterojunction Solar Cells. *Chem. – Eur. J.* **2012**, *18*, 1502–1511, DOI: 10.1002/chem.201102598
28. Zhan, H.-M.; Lamare, S.; Ng, A.; Kenny, T.; Guernon, H.; Chan, W.-K.; Djurisic, A. B.; Harvey, P. D.; Wong, W.-Y. Synthesis and Photovoltaic Properties of New Metalloporphyrin-Containing Polyplatinyne Polymers. *Macromolecules* **2011**, *44*, 5155–5167, DOI: 10.1021/ma2006206
29. Wang, Q.; He, Z.; Wild, A.; Wu, H.; Cao, Y.; Schubert, U. S.; Chui, C.-H.; Wong, W.-Y. Platinum-Acetylide Polymers with Higher Dimensionality for Organic Solar Cells. *Chem. Asian J.* **2011**, *6*, 1766–1777, DOI: 10.1002/asia.201100111
30. Wang, Q.; Wong, W.-Y. New Low-Bandgap Polymetallaynes of Platinum Functionalized with a Triphenylamine-Benzothiadiazole Donor-Acceptor Unit for Solar Cell Applications. *Polym. Chem.* **2011**, *2*, 432–440, DOI: 10.1039/C0PY00273A
31. Wong, W.-Y.; Chow, W.-C.; Cheung, K.-Y.; Fung, M.-K.; Djurisic, A. B.; Chan, W.-K. Harvesting Solar Energy Using Conjugated Metallopolyyne Donors Containing Electron-Rich Phenothiazine-Oligothiophene Moieties. *J. Organomet. Chem.* **2009**, *694*, 2717–2726, DOI: 10.1016/j.jorganchem.2009.02.006
32. Mei, J.; Ogawa, K.; Kim, Y.-G.; Heston, N. C.; Arenas, D. J.; Nasrollahi, Z.; McCarley, T. D.; Tanner, D. B.; Reynolds, J. R.; Schanze, K. S. Low-Band-Gap Platinum Acetylide Polymers as Active Materials for Organic Solar Cells. *ACS Appl. Mater. Interfaces* **2009**, *1*, 150–161, DOI: 10.1021/am800104k
33. Liu, L.; Ho, C.-L.; Wong, W.-Y.; Cheung, K.-Y.; Fung, M.-K.; Lam, W.-T.; Djurisic, A. B.; Chan, W.-K. Effect of Oligothieryl Chain Length on Tuning the Solar Cell Performance in Fluorene-Based Polyplatinyne. *Adv. Funct. Mater.* **2008**, *18*, 2824–2833, DOI: 10.1002/adfm.200800439
34. Guo, F.; Ogawa, K.; Kim, Y.-G.; Danilov, E. O.; Castellano, F. N.; Reynolds, J. R.; Schanze, K. S. A Fulleropyrrolidine End-Capped Platinum-Acetylide Triad: The Mechanism of Photoinduced Charge Transfer in Organometallic Photovoltaic Cells. *Phys. Chem. Chem. Phys.* **2007**, *9*, 2724–2734, DOI: 10.1039/b700379j

35. He, W.; Livshits, M. Y.; Dickie, D. A.; Zhang, Z.; Mejiaortega, L. E.; Rack, J. J.; Wu, Q.; Qin, Y. Impact of “Rollers” on Material Crystallinity, Electronic Properties, and Solar Cell Performance. *J. Am. Chem. Soc.* **2017**, *139*, 14109– 14119, DOI: 10.1021/jacs.7b05801
36. He, W.; Livshits, M. Y.; Dickie, D. A.; Yang, J.; Quinnett, R.; Rack, J. J.; Wu, Q.; Qin, Y. A “Roller-Wheel” Pt-Containing Small Molecule That Outperforms Its Polymer Analogs in Organic Solar Cells. *Chem. Sci.* **2016**, *7*, 5798– 5804, DOI: 10.1039/C6SC00513F
37. Molina-Ontoria, A.; Rivera-Nazario, D. M.; Tigreros, A.; Ortiz, A.; Nunez, J. E.; Insuasty, B.; Lueders, D.; Wolfrum, S.; Guldi, D. M.; Echegoyen, L. Geometric Influence on Intramolecular Photoinduced Electron Transfer in Platinum(II) Acetylide-Linked Donor–Acceptor Assemblies. *Chem. – Eur. J.* **2014**, *20*, 11111– 11119, DOI: 10.1002/chem.201402616
38. Scattergood, P. A.; Delor, M.; Sazanovich, I. V.; Bouganov, O. V.; Tikhomirov, S. A.; Stasheuski, A. S.; Parker, A. W.; Greetham, G. M.; Towrie, M.; Davies, E. S. Electron Transfer Dynamics and Excited State Branching in a Charge-Transfer Platinum(II) Donor-Bridge-Acceptor Assembly. *Dalton Trans.* **2014**, *43*, 17677– 17693, DOI: 10.1039/C4DT01682C
39. Aly, S. M.; Ho, C.-L.; Wong, W.-Y.; Fortin, D.; Harvey, P. D. Intrachain Electron and Energy Transfers in Metal Diynes and Polyynes of Group 10-11 Transition Elements Containing Various Carbazole and Fluorene Hybrids. *Macromolecules* **2009**, *42*, 6902– 6916, DOI: 10.1021/ma9013077
40. Aly, S. M.; Ho, C.-L.; Fortin, D.; Wong, W.-Y.; Abd-El-Aziz, A. S.; Harvey, P. D. Intrachain Electron and Energy Transfer in Conjugated Organometallic Oligomers and Polymers. *Chem. – Eur. J.* **2008**, *14*, 8341– 8352, DOI: 10.1002/chem.200800304
41. Dai, Z.; Metta-Magana, A. J.; Nunez, J. E. Synthesis and Characterization of Electron Donor-Acceptor Platinum(II) Complexes Composed of N,N-Diphenylpyridineamine and Triphenylamine Ligands. *Inorg. Chem.* **2014**, *53*, 7188– 7196, DOI: 10.1021/ic500290m
42. Tigreros, A.; Dhas, V.; Ortiz, A.; Insuasty, B.; Martin, N.; Echegoyen, L. Influence of Acetylene-Linked π -Spacers on Triphenylamine-Fluorene Dye Sensitized Solar Cells Performance. *Sol. Energy Mater. Sol. Cells* **2014**, *121*, 61– 68, DOI: 10.1016/j.solmat.2013.10.035

43. Li, L.; Chow, W.-C.; Wong, W.-Y.; Chui, C.-H.; Wong, R. S.-M. Synthesis, Characterization and Photovoltaic Behavior of Platinum Acetylide Polymers with Electron-Deficient 9,10-Anthraquinone Moiety. *J. Organomet. Chem.* **2011**, *696*, 1189–1197, DOI: 10.1016/j.jorganchem.2010.08.044
44. Li, L.; Sun, X.; Hu, Y.; Wu, Q. Synthesis of a New Platinum Metallopolyyne for Organic Solar Cells. *Adv. Mater. Res.* **2012**, *430–432*, 260–263, DOI: 10.4028/www.scientific.net/AMR.430-432.260
45. Wang, X.; Fortin, D.; Brisard, G.; Harvey, P. D. Drastic Tuning of the Photonic Properties of ‘(Push-Pull)_n’ *trans*-Bis(ethynyl)bis(Tributylphosphine)Platinum(II)-Containing Polymers. *Macromol. Rapid Commun.* **2014**, *35*, 992–997, DOI: 10.1002/marc.201400018
46. Wang, X.; Kenny, T.; Fortin, D.; Aly, S. M.; Brisard, G.; Harvey, P. D. Profound Substituent Effect on the Structural, Optical, Photophysical, and Electrochemical Properties of N,N'-Anthraquinone Diimine-Containing Platinum-Organometallic Polymers. *Organometallics* **2015**, *34*, 1567–1581, DOI: 10.1021/acs.organomet.5b00154
47. Kenny, T.; Aly, S. M.; Fortin, D.; Harvey, P. D. Convenient Tautomeric Forms in an Amino-Anthraquinone Diimine for the Generation of a Mixed-Valent Push-Pull Conjugated Polymer. *Chem. Commun.* **2012**, *48*, 11543–11545, DOI: 10.1039/c2cc36768h
48. Aly, S. M.; Kenny, T.; Lamare, S.; Harvey, P. D. Very Complex Emission Properties of the Pt-Organometallic Versions of PANI. *J. Inorg. Organomet. Polym. Mater.* **2015**, *25*, 118–125, DOI: 10.1007/s10904-014-0109-x
49. Abdelhameed, M.; Langlois, A.; Fortin, D.; Karsenti, P.-L.; Harvey, P. D. Drastic Substituent Effect on the Emission Properties of Quinone diimine Models and Valuable Insight on the Excited States of Emeraldine. *Chem. Commun.* **2014**, *50*, 11214–11217, DOI: 10.1039/C4CC05178E
50. Lamare, S.; Aly, S. M.; Fortin, D.; Harvey, P. D. Incorporation of Zinc(II) Porphyrins in Polyaniline in Its Perigraniline Form Leading to Polymers with the Lowest Band Gap. *Chem. Commun.* **2011**, *47*, 10942–10944, DOI: 10.1039/c1cc14026d
51. Gagnon, K.; Aly, S. M.; Fortin, D.; Abd-El-Aziz, A. S.; Harvey, P. D. The First Organometallic Version of Polyaniline in its Emeraldine Form. *J. Inorg. Organomet. Polym. Mater.* **2009**, *19*, 28–34, DOI: 10.1007/s10904-009-9256-x

52. Fortin, D.; Clement, S.; Gagnon, K.; Berube, J.-F.; Stewart, M. P.; Geiger, W. E.; Harvey, P. D. Conjugated Organometallic Polymer Containing a Redox-Active Center. *Inorg. Chem.* **2009**, *48*, 446–454, DOI: 10.1021/ic800857v
53. Gagnon, K.; Aly, S. M.; Brisach-Wittmeyer, A.; Bellows, D.; Berube, J.-F.; Caron, L.; Abdel-Aziz, A. S.; Fortin, D.; Harvey, P. D. Conjugated Oligomers and Polymers of *cis*- and *trans*-Platinum(II)-para- and ortho-bis(ethynylbenzene)quinone Diimine. *Organometallics* **2008**, *27*, 2201–2214, DOI: 10.1021/om7010563
54. Ueda, M.; Ueno, T.; Suyama, Y.; Ryu, I. Synthesis of 2,3-Disubstituted Indenones by Cobalt-Catalyzed [3+2] Annulation of: O-Methoxycarbonylphenylboronic Acid with Alkynes. *Chem. Commun.* **2016**, *52*, 13237–13240, DOI: 10.1039/C6CC08032D
55. Andre, J. C.; Lopez-Delgado, R.; Lyke, R. L.; Ware, W. R. Calibrating the Light Pulse Shape of a Hydrogen Flashlamp Using Synchrotron Radiation as a Standard of Excitation. *Appl. Opt.* **1979**, *18*, 1355–1359, DOI: 10.1364/AO.18.001355
56. Smith, D. A.; McKenzie, G.; Jones, A. C.; Smith, T. A. Analysis of Time-Correlated Single Photon Counting Data: A Comparative Evaluation of Deterministic and Probabilistic Approaches. *Methods Appl. Fluoresc.* **2017**, *5*, 042001 DOI: 10.1088/2050-6120/aa8055
57. Frisch, M. J.; Trucks, G. W.; Schlegel, H. B.; Scuseria, G. E.; Robb, M. A.; Cheeseman, J. R.; Montgomery, J. A., Jr.; Vreven, T. K. K. N.; Kudin, K. N.; Burant, J. C.; *Gaussian 03*, revision C.02; Gaussian, Inc.: Wallingford, CT, 2009; Vol. 26.
58. Bauernschmitt, R.; Ahlrichs, R. Treatment of Electronic Excitations within the Adiabatic Approximation of Time Dependent Density Functional Theory. *Chem. Phys. Lett.* **1996**, *256*, 454–464, DOI: 10.1016/0009-2614(96)00440-X
59. Becke, A. D. Density-Functional Thermochemistry. III. The Role of Exact Exchange. *J. Chem. Phys.* **1993**, *98*, 5648–5652, DOI: 10.1063/1.464913
60. Casida, M. E.; Jamorski, C.; Casida, K. C.; Salahub, D. R. Molecular Excitation Energies to High-Lying Bound States from Time-Dependent Density-Functional Response Theory: Characterization and Correction of the Time-Dependent Local Density Approximation Ionization Threshold. *J. Chem. Phys.* **1998**, *108*, 4439–4449, DOI: 10.1063/1.475855
61. Hohenberg, P.; Kohn, W. Elementary Excitations in Solids. *Phys. Rev.* **1964**, *136*, B864–B871, DOI: 10.1103/PhysRev.136.B864

62. Kohn, W.; Sham, L. J. Self-Consistent Equations Including Exchange and Correlation Effects. *Phys. Rev.* **1965**, *140*, A1133– A1138, DOI: 10.1103/PhysRev.140.A1133
63. Lee, C.; Yang, W.; Parr, R. G. Development of the Colle-Salvetti Correlation-Energy into a Functional of the Electron Density. *Phys. Rev. B.* **1988**, *37*, 785– 789, DOI: 10.1103/PhysRevB.37.785
64. Miehlich, B.; Savin, A.; Stoll, H.; Preuss, H. Results Obtained with the Correlation Energy Density Functionals of Becke and Lee, Yang and Parr. *Chem. Phys. Lett.* **1989**, *157*, 200– 206, DOI: 10.1016/0009-2614(89)87234-3
65. Parr, R. G.; Yang, W. *Density-Functional Theory of Atoms and Molecules*; Oxford University Press, 1989; Vol. 16.
66. Salahub, D. R.; Zerner, M. C., Eds. *The Challenge of d and f Electrons: Theory and Computation*; American Chemical Society, 1989.
67. Stratmann, R. E.; Scuseria, G. E.; Frisch, M. J. An Efficient Implementation of Time-Dependent Density-Functional Theory for the Calculation of Excitation Energies of Large Molecules. *J. Chem. Phys.* **1998**, *109*, 8218– 8224, DOI: 10.1063/1.477483
68. Binkley, J. S.; Pople, J. A.; Hehre, W. J. Self-Consistent Molecular Orbital Methods. 21. Small Split-Valence Basis Sets for First-Row Elements. *J. Am. Chem. Soc.* **1980**, *102*, 939– 947, DOI: 10.1021/ja00523a008
69. Dobbs, K. D.; Hehre, W. J. Molecular Orbital Theory of the Properties of Inorganic and Organometallic Compounds 4. Extended Basis Sets for Third-and Fourth-Row, Main-Group Elements. *J. Comput. Chem.* **1986**, *7*, 359– 378, DOI: 10.1002/jcc.540070313
70. Dobbs, K. D.; Hehre, W. J. Molecular Orbital Theory of the Properties of Inorganic and Organometallic Compounds 5. Extended Basis Sets for First-Row Transition Metals. *J. Comput. Chem.* **1987**, *8*, 861– 879, DOI: 10.1002/jcc.540080614
71. Dobbs, K. D.; Hehre, W. J. Molecular Orbital Theory of the Properties of Inorganic and Organometallic Compounds. 6. Extended Basis Sets for Second-Row Transition Metals. *J. Comput. Chem.* **1987**, *8*, 880– 893, DOI: 10.1002/jcc.540080615
72. Gordon, M. S.; Binkley, J. S.; Pople, J. A.; Pietro, W. J.; Hehre, W. J. Self-Consistent Molecular-Orbital Methods. 22. Small Split-Valence Basis Sets for Second-Row Elements. *J. Am. Chem. Soc.* **1982**, *104*, 2797– 2803, DOI: 10.1021/ja00374a017

73. Pietro, W. J.; Francel, M. M.; Hehre, W. J.; DeFrees, D. J.; Pople, J. A.; Binkley, J. S. Self-Consistent Molecular Orbital Methods. 24. Supplemented Small Split-Valence Basis Sets for Second-Row Elements. *J. Am. Chem. Soc.* **1982**, *104*, 5039–5048, DOI: 10.1021/ja00383a007
74. O'boyle, N. M.; Tenderholt, A. L.; Langner, K. M. CcLib: A Library for Package-Independent Computational Chemistry Algorithms. *J. Comput. Chem.* **2008**, *29*, 839–845, DOI: 10.1002/jcc.20823
75. Liu, Y.; Jiang, S.; Glusac, K.; Powell, D. H.; Anderson, D. F.; Schanze, K. S. Photophysics of Monodisperse Platinum-Acetylide Oligomers: Delocalization in the Singlet and Triplet Excited States. *J. Am. Chem. Soc.* **2002**, *124*, 12412–12413, DOI: 10.1021/ja027639i
76. Choi, J.; Ahn, D. S.; Oang, K. Y.; Cho, D. W.; Ihee, H. Charge Transfer-Induced Torsional Dynamics in the Excited State of 2, 6-Bis (diphenylamino) anthraquinone. *J. Phys. Chem. C* **2017**, *121*, 24317–24323, DOI: 10.1021/acs.jpcc.7b07553
77. Marineau-Plante, G.; Juvenal, F.; Langlois, A.; Fortin, D.; Soldera, A.; Harvey, P. D. Multiply “Trapped” ³[*trans*-Pt(PR₃)₂(C≡CC₆H₄X)₂]* Conformers in Rigid Media. *Chem. Commun.* **2018**, *54*, 976–979, DOI: 10.1039/C7CC09503A
78. Marineau Plante, G.; Fortin, D.; Soldera, A.; Harvey, P. D. Solid-Solid Phase Transitions in [*trans*-Pt(PMe₃)₂(C≡CC₆H₄R)₂]-Containing Materials (R = O(CH₂)_nH; n = 6, 9, 12, and 15). *Organometallics* **2018**, *37*, 2544–2552, DOI: 10.1021/acs.organomet.8b00304
79. Matsuo, Y. Fullerene Derivatives as Electron Acceptors in Polymer Solar Cells. *RSC Polym. Chem. Ser.* **2016**, *17*, 78–100, DOI: 10.1039/9781782622307-00078
80. Cook, S.; Katoh, R.; Furube, A. Ultrafast Studies of Charge Generation in PCBM: P3HT Blend Films following Excitation of the Fullerene PCBM. *J. Phys. Chem. C* **2009**, *113*, 2547–2552, DOI: 10.1021/jp8050774
81. Kreher, D.; Cariou, M.; Liu, S.-G.; Levillain, E.; Veciana, J.; Rovira, C.; Gorgues, A.; Hudhomme, P. Rigidified Tetrathiafulvalene-[60]Fullerene Assemblies: Towards the Control of Through-Space Orientation between Both Electroactive Units. *J. Mater. Chem.* **2002**, *12*, 2137–2159, DOI: 10.1039/b201695h
82. Zhao, G.; He, Y.; Xu, Z.; Hou, J.; Zhang, M.; Min, J.; Chen, H.-Y.; Ye, M.; Hong, Z.; Yang, Y.; Li, Y. Effect of Carbon Chain Length in the Substituent of PCBM-like Molecules on

- Their Photovoltaic Properties. *Adv. Funct. Mater.* **2010**, *20*, 1480–1487, DOI: 10.1002/adfm.200902447
83. Turro, N. J.; Ramamurthy, V.; Scaiano, J. C. *Modern Molecular Photochemistry of Organic Molecules*; University Science Books: Sausalito, CA, 2010.
84. Cook, S.; Furube, A.; Katoh, R.; Han, L. Estimate of Singlet Diffusion Lengths in PCBM Films by Time-Resolved Emission Studies. *Chem. Phys. Lett.* **2009**, *478*, 33–36, DOI: 10.1016/j.cplett.2009.06.091
85. Dogru, M.; Handloser, M.; Auras, F.; Kunz, T.; Medina, D.; Hartschuh, A.; Knochel, P.; Bein, T. A Photoconductive Thienothiophene-Based Covalent Organic Framework Showing Charge Transfer Towards Included Fullerene. *Angew. Chem.* **2013**, *125*, 2992–2996, DOI: 10.1002/ange.201208514
86. Pandit, B.; Gautam, B. R.; Basel, T. P.; Vardeny, Z. V. Correlation Between Ultrafast Transient Photomodulation Spectroscopy and Organic Photovoltaic Solar Cell Efficiency Based on RR-P3HT/PCBM Blends. *Org. Electron.* **2014**, *15*, 1149–1154, DOI: 10.1016/j.orgel.2014.03.021
87. Jespersen, K. G.; Zhang, F.; Gadisa, A.; Sundstroem, V.; Yartsev, A.; Inganaes, O. Charge Formation and Transport in Bulk-Heterojunction Solar Cells Based on Alternating Polyfluorene Copolymers Blended with Fullerenes. *Org. Electron.* **2006**, *7*, 235–242, DOI: 10.1016/j.orgel.2006.03.001
88. Keiderling, C.; Dimitrov, S.; Durrant, J. R. Exciton and Charge Generation in PC60BM Thin Films. *J. Phys. Chem. C* **2017**, *121*, 14470–14475, DOI: 10.1021/acs.jpcc.7b03962
89. Causa, M.; Ramirez, I.; Hardigree, J. F. M.; Riede, M.; Banerji, N. Femtosecond Dynamics of Photoexcited C60 Films. *J. Phys. Chem. Lett.* **2018**, *9*, 1885–1892, DOI: 10.1021/acs.jpcl.8b00520
90. Srivani, D.; Gupta, A.; Bhosale, S. V.; Ohkubo, K.; Bhosale, R. S.; Fukuzumi, S.; Bilic, A.; Jones, L. A.; Bhosale, S. V. A Triphenylamine-Naphthalenediimide-Fullerene Triad: Synthesis, Photoinduced Charge Separation and Solution-Processable Bulk Heterojunction Solar Cells. *Asian J. Org. Chem.* **2018**, *7*, 220–226, DOI: 10.1002/ajoc.201700557

91. Unger, T.; Wedler, S.; Kahle, F.-J.; Scherf, U.; Baessler, H.; Koehler, A. The Impact of Driving Force and Temperature on the Electron Transfer in Donor-Acceptor Blend Systems. *J. Phys. Chem. C* **2017**, *121*, 22739– 22752, DOI: 10.1021/acs.jpcc.7b09213
92. Jakowetz, A. C.; Bohm, M. L.; Zhang, J.; Sadhanala, A.; Huettner, S.; Bakulin, A. A.; Rao, A.; Friend, R. H. What Controls the Rate of Ultrafast Charge Transfer and Charge Separation Efficiency in Organic Photovoltaic Blends. *J. Am. Chem. Soc.* **2016**, *138*, 11672– 11679, DOI: 10.1021/jacs.6b05131
93. Wright, B. F.; Sunahara, K.; Furube, A.; Nattestad, A.; Clarke, T. M.; Bazan, G. C.; Azoulay, J. D.; Mozer, A. J. Driving Force Dependence of Electron Transfer Kinetics and Yield in Low-Band-Gap Polymer Donor-Acceptor Organic Photovoltaic Blends. *J. Phys. Chem. C* **2015**, *119*, 12829– 12837, DOI: 10.1021/acs.jpcc.5b01617
94. Rodovsky, D. B.; Peet, J.; Shao, N.; Azoulay, J. D.; Bazan, G. C.; Drolet, N.; Wu, Q.; Sfeir, M. Y. Quantifying the Relationship between the Maximum Achievable Voltage and Current Levels in Low-Bandgap Polymer Photovoltaics. *J. Phys. Chem. C* **2013**, *117*, 25955– 25960, DOI: 10.1021/jp410234u

Graphical Abstract

